CERN-ACC-2018-0009

Galina.Skripka@cern.ch

Beam-induced heat loads on the beam screens of the inner triplets for the HL-LHC

G. Skripka and G. Iadarola
CERN, Geneva, Switzerland

Keywords: LHC, HL-LHC, heat load, triplet, beam screen, impedance, electron cloud

Abstract

The expected heat load induced on the beam screens has been evaluated for the triplet assemblies in the four experimental Insertion Regions (IRs) of the HL-LHC. The contribution from electron cloud effects has been estimated using PyECLOUD macroparticle simulations. The presence of a surface treatment for the reduction of the Secondary Electron Yield has been taken into account. The contribution from the impedance of the beam screen has been evaluated taking into account the impact of the temperature and of the magnetic field on the resistivity of the surface.

Geneva, Switzerland
February 2018

1 Introduction

The operation of the Large Hadron Collider (LHC) with 25 ns bunch spacing during Run 2 has shown that beam induced heat loads on the beam screens of the cold magnets can pose serious limitations to the achievable machine performance [1, 2]. It is therefore important to assess the potential impact that these effects could have in the High Luminosity LHC (HL-LHC) era [3].
In a previous document [4] estimates for the heat loads expected on the beam screens of the twin-bore magnets in all the Insertion Regions (IRs) were provided. Here we perform similar calculations for the Inner Triplets installed on each side of the four experimental Interaction Points (IPs).
While the inner triplets installed in IR2 and IR8 will not be changed, those presently installed in IR1 and IR5 will be replaced with a newly designed version sketched in Fig. 1 [3].
The two main sources of beam-induced heat load on the beam screens are impedance heating and electron cloud (e-cloud) effects, as the power deposition from synchrotron radiation was found to be negligible by previous studies [5–7]. In the absence of any countermeasure the load from e-cloud is expected to be very large. For this reason a surface treatment will be applied to the beam screen of all triplet assemblies in order to reduce its Secondary Electron Yield (SEY) and therefore mitigate the e-cloud formation [3]. According to the present baseline, coating with amorphous carbon will be used for this purpose.
The e-cloud induced heat loads have been estimated as a function of the SEY of the surface using PyECLOUD [8] macroparticle simulations. The power deposition from impedance has been computed analytically, following the approach presented in [4].

2 Electron cloud build-up simulations

Electron cloud build-up simulations were performed for the inner triplets on the right side of IP5 and IP8. Due to symmetry considerations, the results are applicable to the similar devices installed on the other sides and at the IP1 and IP2 respectively. The required information on the triplet geometry was retrieved from the CERN Drawing Directory [9] for IR5 and from the LHC design report [10] for IR8. The main beam parameters used in the simulations are reported in Table 1. A sufficiently long portion of the beam (576 or 864 bunches) has been simulated in order to reach the saturation of the e-cloud at all sections where multipacting occurs. All results presented in the following are re-scaled to the full number of bunches (2748 bunches).
To correctly model the presence of two counter-rotating beams in the same chamber, we simulate different slices along the triplet, correctly accounting for different arrival times, transverse sizes and transverse positions of the two beams at each section. The simulated slices are chosen with a 1 m step for the long components of the triplet. For the elements of shorter length, such as correctors and some of the drifts, the e-cloud is simulated at the central section.

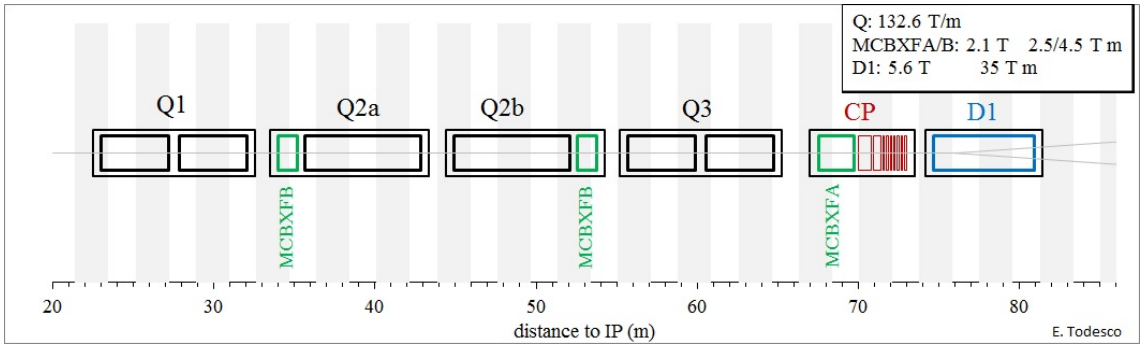

Figure 1: Schematic of the HL-LHC triplet layout for IR1 and IR5 (drawing from [11]). Q1, Q2a, Q2b, Q3 are quadrupole magnets, D1 is the separation/recombination dipole, MCBXFA/B are dipole correctors and CP is the higher order corrector package.

Table 1: Simulation parameters.

Energy, TeV	7
Intensity, p/bunch	2.2×10^{11}
RMS bunch length (Gaussian), m	0.09
Bunch spacing, ns	25
Optics	HL-LHC v1.2 (β^*=15 cm)
Number of bunches	2×288 or 3×288 [1]

[1] three trains used for simulations for which the e-cloud has not reached it saturation during the passage of the first two trains.

Simulations were performed for all sections and for different values of the SEY parameter (δ_{max}) uniformly spaced in the range 1.0-1.6. Snapshots of the e-cloud distribution for the different magnetic elements are reported in Appendix A. The heat loads in all simulations were calculated using the data only from the last simulated bunch train. The dependence of the heat load on the SEY at each simulated section is reported in Appendix B for the triplet in IR5 and in Appendix C for the triplets in IR8.
Figure 2 shows the total expected heat load from e-cloud as a function of the SEY parameter under the assumption that the beam screen has the same surface properties over the entire length. In these estimates, the multipole correctors are assumed to be off and therefore are simulated as field free regions.
In the following we will analyze more in detail the simulation results for two different SEY values:

- SEY=1.3, corresponding to a copper surface after beam conditioning, i.e. the configuration of the present LHC inner triplets;
- SEY=1.1, as it can be obtained with surface treatments (e.g. amorphous carbon coating, for which even lower SEY values can be achieved [12]).

For these two SEY values, the heat load distribution along the inner triplets are compared in Figs. 3 and 4. In these figures the dashed vertical lines mark the

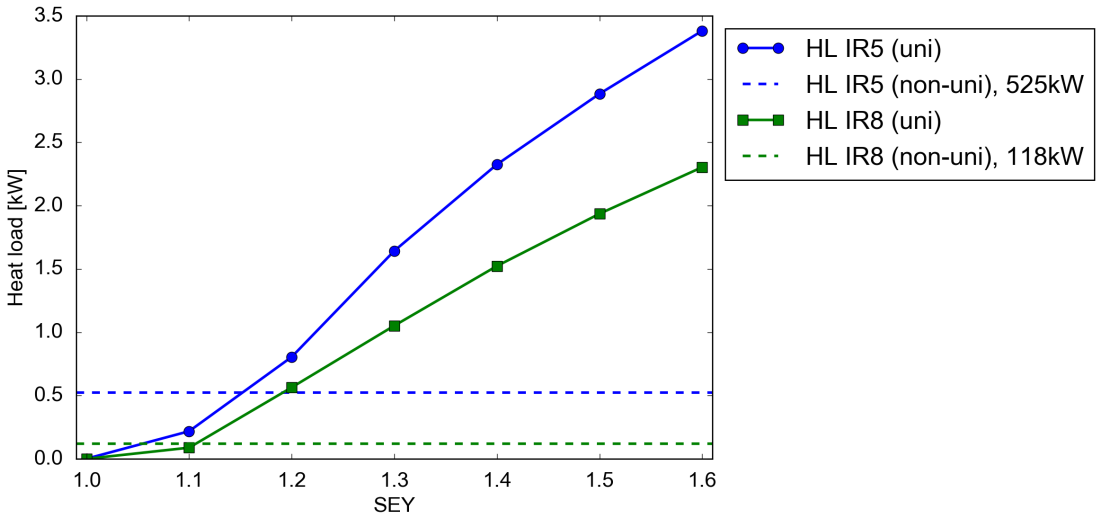

Figure 2: Total heat load as a function of the SEY for the inner triplets in IR5 and in IR8. The dashed lines mark the heat load in the cases of non-uniform coating (SEY=1.3 in the drift sections outside the cold masses, SEY=1.1 elsewhere).

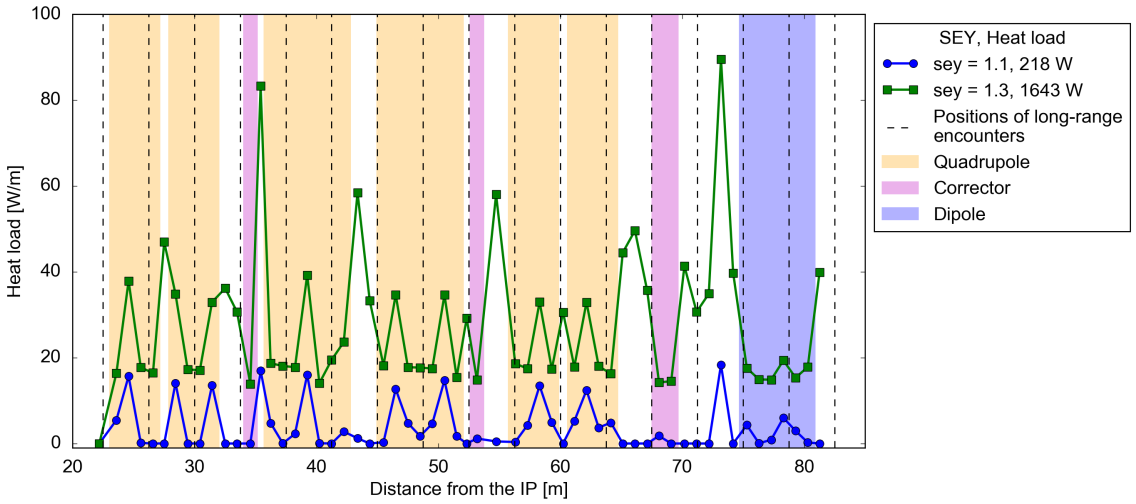

Figure 3: Heat load along one of the IR5 triplets for two values of the SEY parameter. The colored areas mark different magnetic field configurations as indicated in the legend.

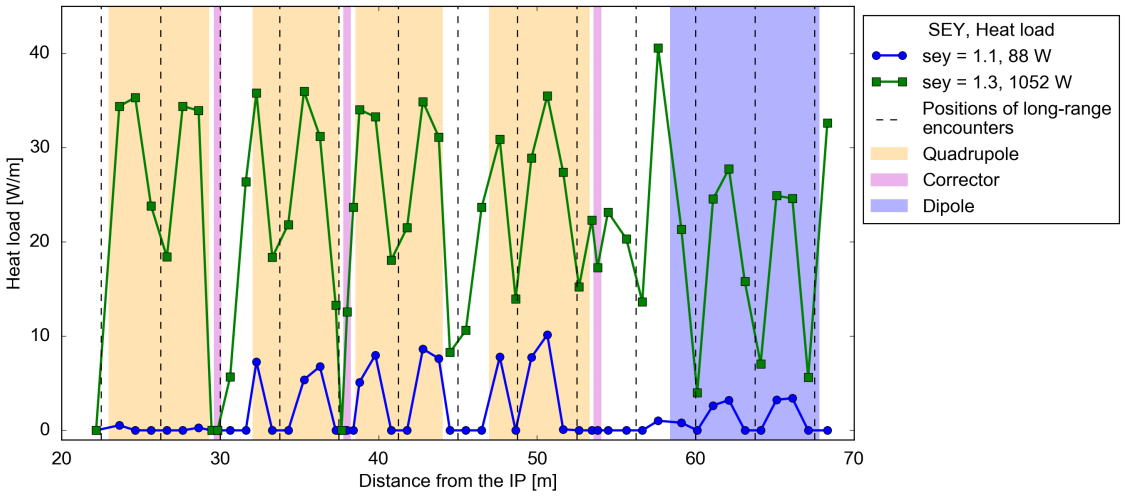

Figure 4: Heat load along one of the IR8 triplets for two values of the SEY parameter. The colored areas mark different magnetic field configurations as indicated in the legend.

locations of long-range encounters (LREs), where bunches of the two beams pass at the same time. The heat load tends to be larger at locations between the LREs. Large peaks are observed at some of the drift sections.
For both devices the heat load expected in absence of surface treatment is very high, in the order of 1 kW, but a significant heat load reduction (one order of magnitude or larger) is observed for the coated case.

2.1 Effect of higher SEY in the drift sections

Due to technical difficulties, the surface coating with amorphous carbon might not be applied to some short components in the drifts sections located outside the cold masses, like the beam position monitors and the deformable bellows.
In order to assess the impact of this scenario, the total heat load for the triplet assemblies has been evaluated in the conservative hypothesis in which all drifts situated outside the cold masses are not coated and therefore have SEY parameter of 1.3 (see drawing in Fig 5). The total heat loads obtained with these SEY configurations are indicated by the dashed horizontal lines in Fig. 2. The impact of having uncoated drifts is stronger for the triplets in IR5, for which the heat load increase compared to the fully coated case is in the order of 300 W. The effect for the triplets in IR8 is, instead, quite limited. Figures 6 and 7 show the heat load distribution along the triplets under these assumptions. The uncoated drifts are indicated with the green background color. One can notice that the heat load density in these regions is significantly larger compared to the coated sections.

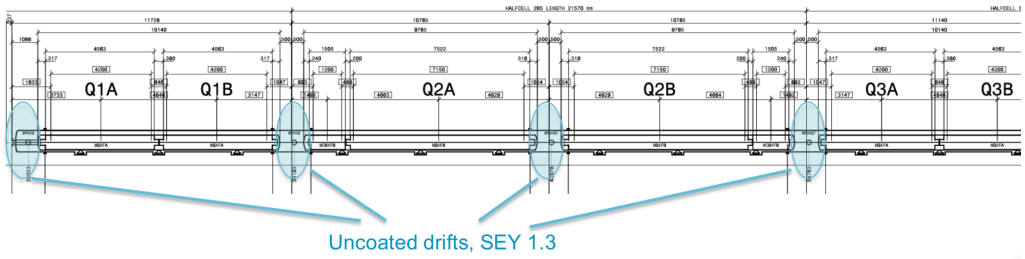

Figure 5: Schematic drawing of a triplet showing the uncoated drifts outside cold masses.

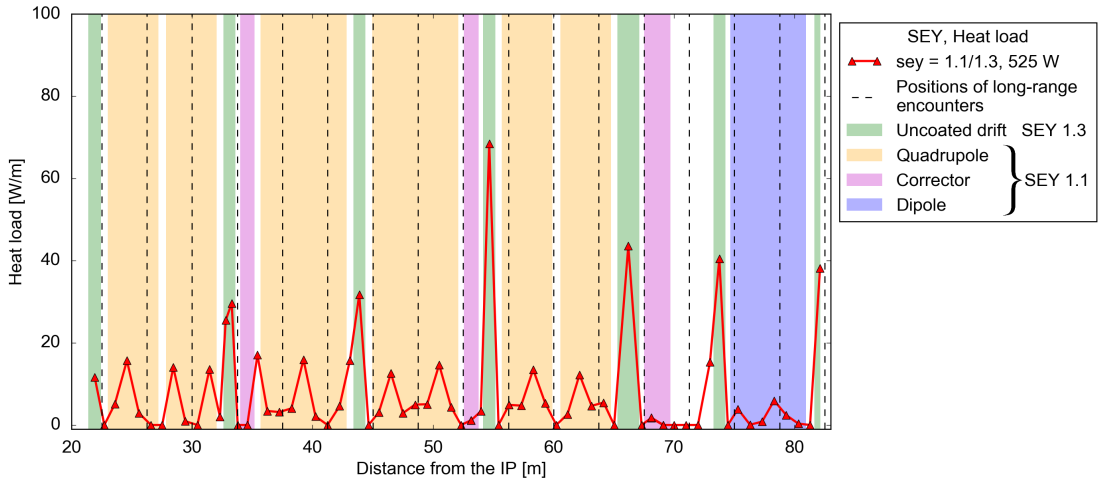

Figure 6: Heat load along one of the IR5 triplets in the case in which the drift spaces outside the cold masses are not coated. The colored areas mark different magnetic field and SEY configurations as indicated in the legend.

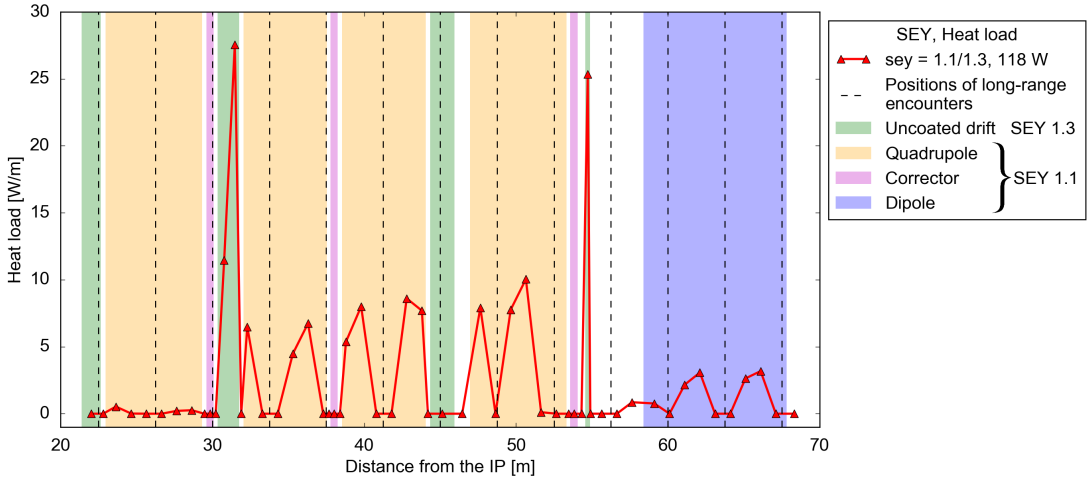

Figure 7: Heat load along one of the IR8 triplets in the case in which the drift spaces outside the cold masses are not coated. The colored areas mark different magnetic field configuration as indicated in the legend.

2.2 Effect of high-order corrector magnets

A set of multipole correctors, including sextupole, octupole, decapole and dodecapole magnets (normal and skew), is located between the Q3 and the D1 magnets. This will be used in operation only for IR1 and IR5.
Recently, the possibility of simulating high order multipoles has been introduced in the PyECLOUD simulation code [13]. This allowed performing simulations for the triplet multipole correctors, including the effect of the two counter-rotating beams in the same chamber. The nominal settings of the multipole correctors (included in the optics file) were used for the simulations.
The simulated heat load for each corrector as a function of the SEY of the surface is reported in Appendix B (Figs. B.22 to B.29). Snapshots of the e-cloud distribution in the presence of the multipolar magnetic fields are presented in Appendix A (Figs. A.5 to A.8).
Figure 8 shows the longitudinal distribution of the e-cloud-induced heat load including the effect of the multipole correctors. As the multipacting threshold for the multipoles is larger than for the corresponding drift, a slightly beneficial effect on the heat loads is observed. The total heat load is reduced from 525 W to 514 W when the corrector package is in place.

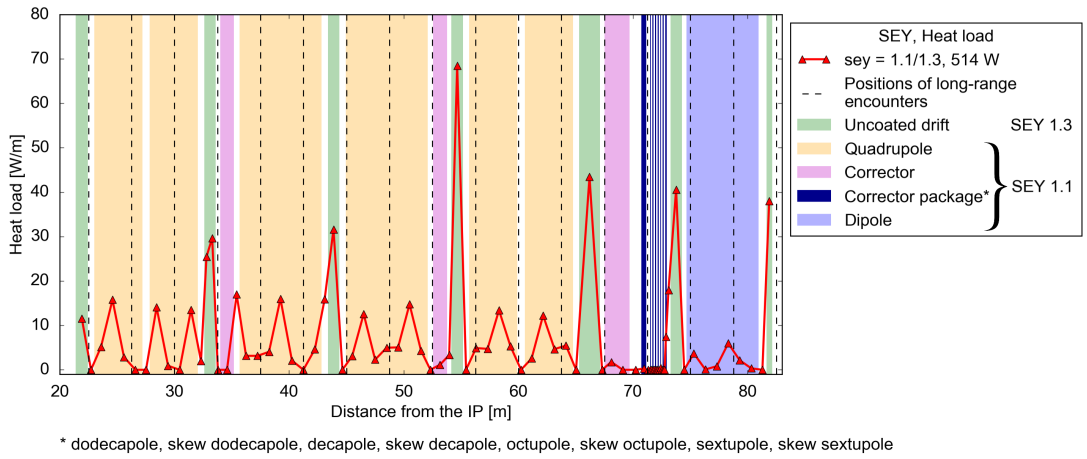

Figure 8: Heat load along one of the IR5 triplets in the case in which the drift spaces outside the cold masses are not coated, including the effect of the e-cloud in the multipole correctors. The colored areas mark different magnetic field configuration as indicated in the legend.

3 Total expected heat loads

In order to evaluate the total expected heat loads on the beam screens, the estimates from e-cloud effects presented in the previous sections need to be combined with heat load estimations from impedance heating. The latter have been evaluated following the procedure described in [4], which has been validated against measurements at the LHC.

Name	Length	Field config.	Chamber	Impedance (T_BS=70 K)	e-cloud (SEY=1.1/1.3(UncDrifts))	Total
ITQ1R5	11.6 m		BSHL_Q1	4.1 W	78.5 W	82.6 W
MQXFA.A1R5	4.2 m	quad	BSHL_Q1	1.5 W	25.0 W	
MQXFA.B1R5	4.2 m	quad	BSHL_Q1	1.5 W	29.9 W	
Drifts	1.7 m	drift	BSHL_Q1	0.6 W	1.1 W	
UncoatedDrifts	1.5 m	drift	BSHL_Q1	0.5 W	**22.5 W**	
ITQ2Q3R5	49.1 m		BSHL_Q23	15.3 W	434.4 W	449.7 W
MQXFB.A2R5	7.2 m	quad	BSHL_Q23	2.3 W	33.8 W	
MQXFB.B2R5	7.2 m	quad	BSHL_Q23	2.3 W	48.1 W	
MQXFA.A3R5	4.2 m	quad	BSHL_Q23	1.3 W	29.7 W	
MQXFA.B3R5	4.2 m	quad	BSHL_Q23	1.3 W	26.2 W	
MBXF.4R5	6.3 m	dip	BSHL_Q23	2.0 W	13.6 W	
MCBXFBV.A2R5	1.2 m	dip	BSHL_Q23	0.4 W	0.0 W	
MCBXFBH.A2R5						
MCBXFBV.B2R5	1.2 m	dip	BSHL_Q23	0.4 W	1.4 W	
MCBXFBH.B2R5						
MCBXFAV.3R5	2.2 m	dip	BSHL_Q23	0.7 W	1.9 W	
MCBXFAH.3R5						
MCTXF.3R5	0.4 m	dodecap	BSHL_Q23	0.1 W	0.1 W	
MCTSXF.3R5	0.1 m	skew dodecap	BSHL_Q23	0.0 W	0.0 W	
MCDXF.3R5	0.1 m	decap	BSHL_Q23	0.0 W	0.0 W	
MCDSXF.3R5	0.1 m	skew decap	BSHL_Q23	0.0 W	0.0 W	
MCOXF.3R5	0.1 m	oct	BSHL_Q23	0.0 W	0.0 W	
MCOSXF.3R5	0.1 m	skew oct	BSHL_Q23	0.0 W	0.0 W	
MCSXF.3R5	0.1 m	sext	BSHL_Q23	0.0 W	0.0 W	
MCSSXF.3R5	0.1 m	skew sext	BSHL_Q23	0.0 W	0.8 W	
Drifts	8.6 m	drift	BSHL_Q23	2.6 W	24.3 W	
UncoatedDrifts	5.9 m	drift	BSHL_Q23	1.8 W	**255.4 W**	
Total IT R5						**532.4 W**

Table 2: Expected heat loads for the different elements of the inner triplet installed on the right side of IP5. Contribution from uncoated drifts marked in bold.

A copper layer is applied on the stainless steel beam screen to lower its longitudinal impedance. The presence of the thin layer of amorphous carbon, applied on top of the copper layer for e-cloud mitigation, was shown to have no impact on the real part of the longitudinal impedance and therefore on impedance heating [14]. The effect of the beam screen temperature (assumed to be 70 K for the triplets in IR1 and IR5 and 20 K for the triplets in IR2 and IR8) on the copper resistivity has been taken into account, together with the effects of the applied magnetic field and the longitudinal weld of the screen.
A summary of all expected heat loads on the beam screens of the Inner Triplets is presented in Tables 2 and 3. To evaluate the e-cloud contribution, SEY=1.3 is assumed for the drifts outside the cold masses and SEY=1.1 is assumed for the rest of the triplet length. For the inner triplets in IR1 and IR5, the effect of the multipole magnetic correctors is taken into account.
Under these assumptions, the total heat load is 532 W for the inner triplets in IR5

Name	Length	Field config.	Chamber	Impedance (T_BS= 20 K)	e-cloud (SEY=1.1/1.3(UncDrifts))	Total
ITQ1R8	9.8 m		BSMQ_Q1-R	5.2 W	10.7 W	15.9 W
MQXA.1R8	6.4 m	quad	BSMQ_Q1-R	3.5 W	1.1 W	
MCBXH.1R8						
MCBXV.1R8	0.5 m	dip	BSMQ_Q1-R	0.2 W	0.0 W	
Drifts	0.9 m	drift	BSMQ_Q1-R	0.4 W	0.0 W	
UncoatedDrifts	2.1 m	drift	BSMQ_Q1-R	1.0 W	**9.6 W**	
ITQ2Q3R8	23.7 m		BSMQ_2	9.3 W	94.2 W	103.5 W
MQXB.A2R8	5.5 m	quad	BSMQ_2	2.3 W	16.2 W	
MQXB.B2R8	5.5 m	quad	BSMQ_2	2.3 W	27.2 W	
MQXA.3R8	6.4 m	quad	BSMQ_2	2.6 W	27.5 W	
MCBXH.2R8						
MCBXV.2R8	0.5 m	dip	BSMQ_2	0.2 W	0.0 W	
MCBXH.3R8						
MCBXV.3R8	0.5 m	dip	BSMQ_2	0.2 W	0.0 W	
Drifts	2.9 m	drift	BSMQ_2	1.0 W	0.0 W	
UncoatedDrifts	2.5 m	drift	BSMQ_2	0.8 W	**23.4 W**	
ITD1R8	13.9 m		BSMB_1	4.2 W	13.4 W	17.6 W
MBX.4R8	9.5 m	dip	BSMB_1	3.0 W	12.4 W	
Drifts	4.4 m	drift	BSMB_1	1.2 W	1.0 W	
UncoatedDrifts	0.0 m	drift	BSMB_1	0.0 W	**0.0 W**	
Total IT R8						**137.0 W**

Table 3: Expected heat loads for the different elements of the inner triplet installed on the right side of IP8. Contribution from uncoated drifts marked in bold.

(same in IR1) and 137 W in IR8 (same in IR2). One can notice that the heat loads are dominated by the contribution of the e-cloud in the uncoated drifts.
Additional tables for the ideal cases of the fully coated and fully uncoated beam screens are included in Appendix D.

4 Summary and conclusions

The beam-induced heat loads on the beam screen in the triplet assemblies of the HL-LHC have been estimated taking into account the contributions from e-cloud effects and from impedance heating.
The e-cloud component has been studied with macroparticle simulations performed with the PyECLOUD code. Several sections of the devices were simulated in order to correctly account for the presence of the two counter-rotating beams in the same chamber. The simulation results show that the presence of the amorphous carbon coating (or of an equivalent surface treatment) results in a reduction of the heat load by more than one order of magnitude. The impact of not coating the drift sections between the cold masses (where bellows and beam position monitors are located) has been evaluated. The e-cloud formation in multipole corrector magnets has been simulated and taken into account in the heat

load estimates.
Combining the e-cloud simulation results with analytic estimates of the impedance heating, which have been checked during the LHC operation, tables with the total expected heat loads for all the elements of the triplet assemblies have been compiled. The total heat loads for different coating scenarios are presented in Table 4. For the entire triplet assembly it amounts to 532 W in IR5 (same in IR1) and to 137 W for in IR8 (same in IR2).

Table 4: Heat loads in IR5 and IR8 for different coating scenarios.

	Fully-coated (SEY=1.1)	Non-uniform coating[1]	Uncoated (SEY=1.3)
IR5	238 W	532 W	1663 W
IR8	107 W	137 W	1071 W

[1] the drifts outside the cold masses are uncoated (SEY 1.3) and the rest of the beam screen is coated (SEY 1.1)

Acknowledgments

The authors would like to thank G. Arduini, P. Dijkstal, E. Métral, A. Romano and G. Rumolo for their important input provided to the presented studies.

Appendix A

Electron cloud distribution in the different components

Animations of the electron dynamics during the passage of two consecutive bunches for SEY 1.3 and locations far from the LREs can be found in [15–28]. Selected snapshots are reported in the following. The asymmetry of the e-cloud distribution observed in some of the snapshots is due to the non symmetric position of the circulating beams within the chambers.

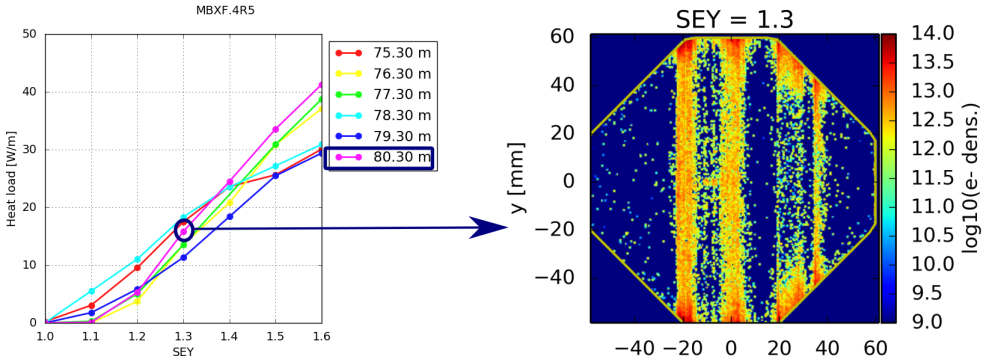

Figure A.1: Heat load vs SEY for different slices along the IR5 D1 dipole magnet (left). Distribution of electrons inside the chamber (right) at the location in between two long range encounters for $SEY = 1.3$.

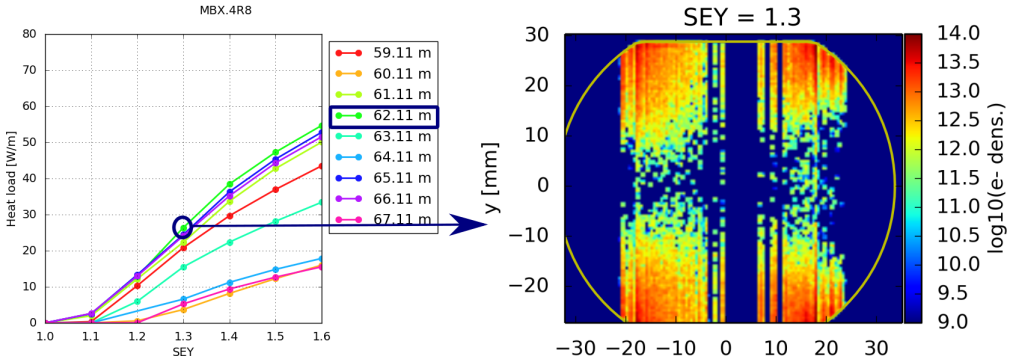

Figure A.2: Heat load vs SEY for different slices along the IR8 D1 dipole magnet (left). Distribution of electrons inside the dipole chamber (right) at the location in between two long range encounters for $SEY = 1.3$.

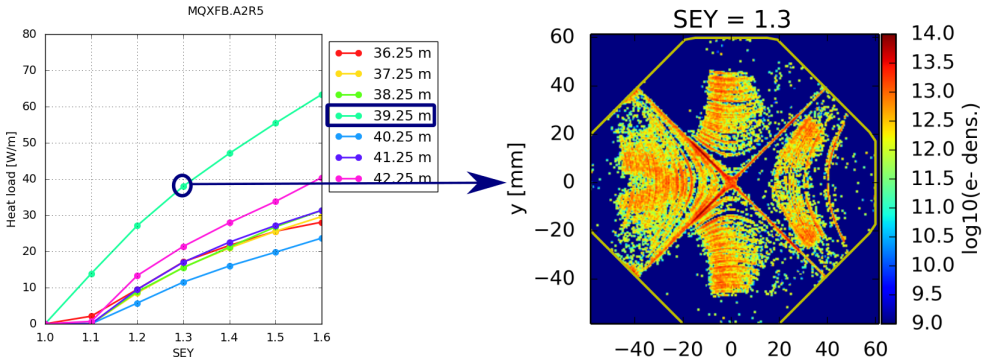

Figure A.3: Heat load vs SEY for different slices along the IR5 Q2a quadrupole magnet (left). Distribution of electrons inside the chamber (right) at the location in between two long range encounters for $SEY = 1.3$.

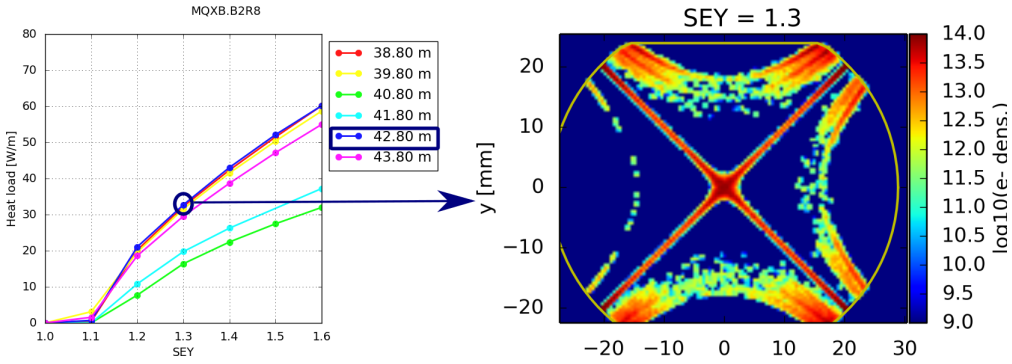

Figure A.4: Heat load vs SEY for different slices along the IR8 Q2a quadrupole magnet (left). Distribution of electrons inside the chamber (right) at the location in between two long range encounters for $SEY = 1.3$.

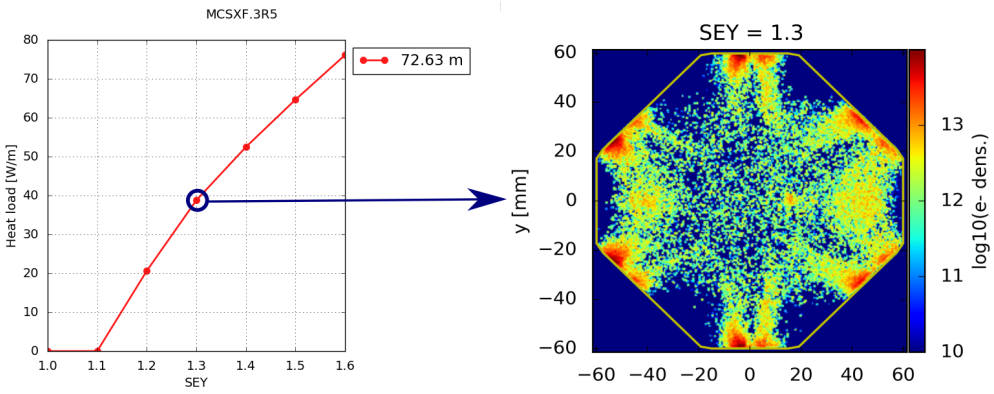

Figure A.5: Heat load vs SEY in the IR5 sextupole magnet within the triplet corrector package (left). Distribution of electrons inside the chamber (right) for $SEY = 1.3$.

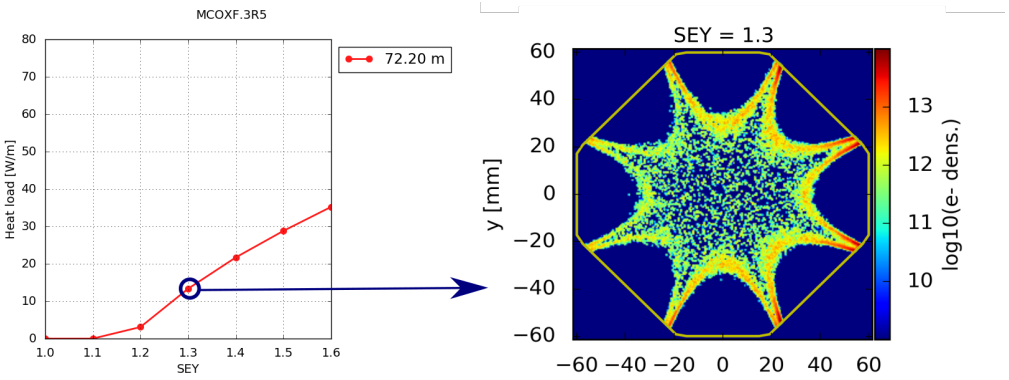

Figure A.6: Heat load vs SEY in the IR5 octupole magnet within the triplet corrector package (left). Distribution of electrons inside the chamber (right) for $SEY = 1.3$.

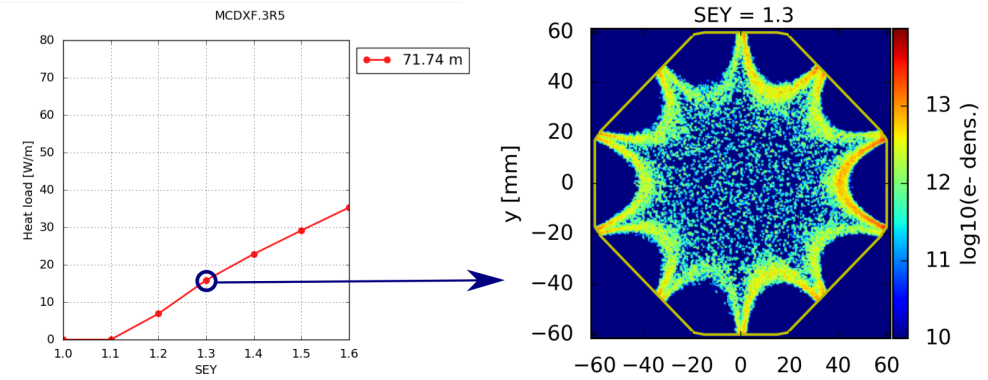

Figure A.7: Heat load vs SEY in the IR5 decapole magnet within the triplet corrector package (left). Distribution of electrons inside the chamber (right) for $SEY = 1.3$.

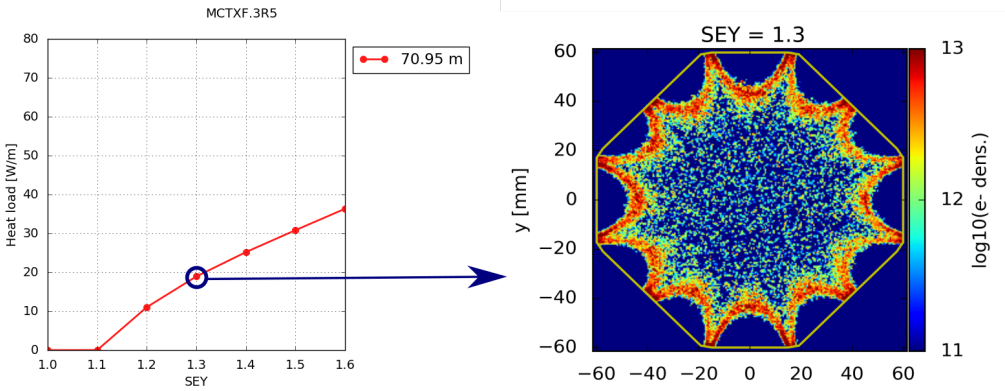

Figure A.8: Heat load vs SEY in the IR5 dodecapole magnet within the triplet corrector package (left). Distribution of electrons inside the chamber (right) for $SEY = 1.3$.

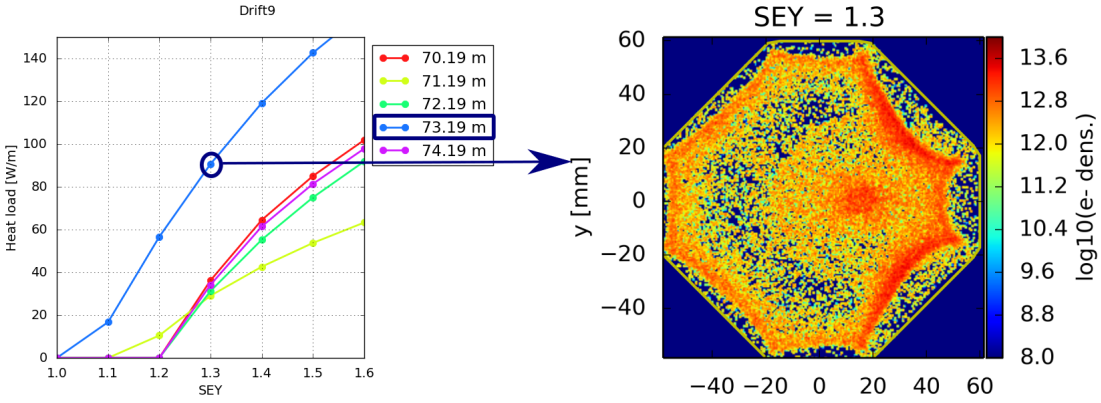

Figure A.9: Heat load vs SEY for different slices along the IR5 drift (left). Distribution of electrons inside the chamber (right) at the location in between two long range encounters for $SEY = 1.3$.

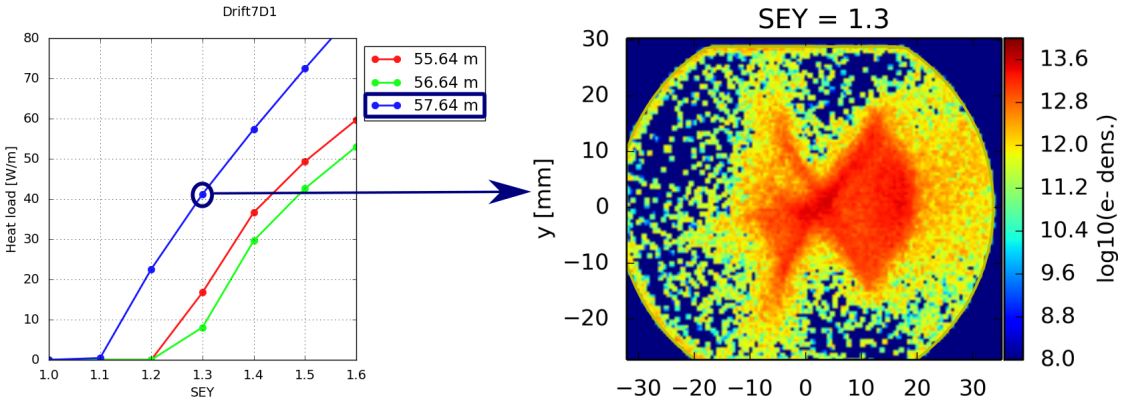

Figure A.10: Heat load vs SEY for different slices along the IR8 drift (left). Distribution of electrons inside the chamber (right) at the location in between two long range encounters for $SEY = 1.3$.

Appendix B

Heat load vs SEY for all simulated sections of the triplets in IR1 and IR5

In the following we report the heat load as a function of the SEY for all simulated sections of the triplet in IR5 (same in IR1). A schematic layout of the triplet is displayed in Fig B.1. The different elements are numbered and the corresponding names are reported in Tab. B.1. The simulated sections are marked by vertical black lines. The vertical blue lines indicate the locations where a change in the beam screen geometry takes place.

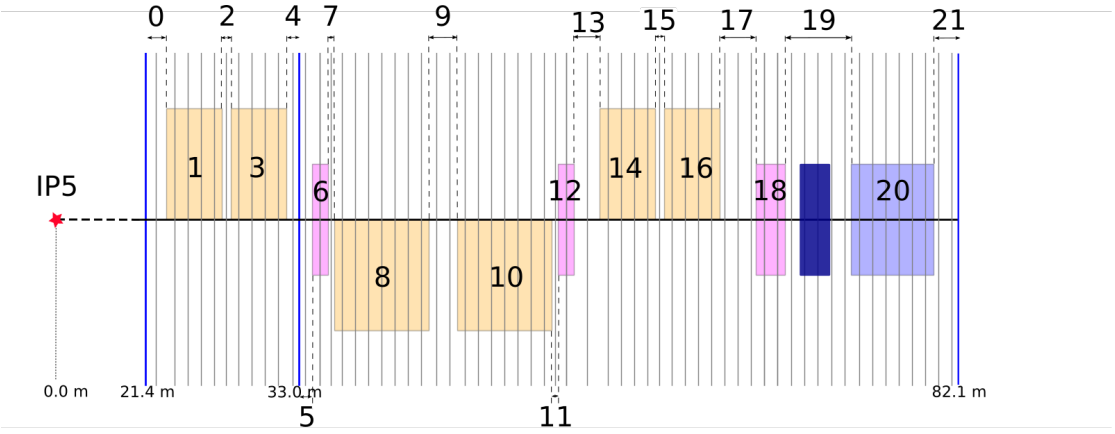

0. Drift0
1. MQXFA.A1R5
2. Drift1
3. MQXFA.B1R5
4. Drift2Q1
5. Drift2Q2Q3
6. MCBXFBV.A2R5/ MCBXFBH.A2R5
7. Drift3
8. MQXFB.A2R5
9. Drift4
10. MQXFB.B2R5
11. Drift5
12. MCBXFBV.B2R5/ MCBXFBH.B2R5
13. Drift6
14. MQXFA.A3R5
15. Drift7
16. MQXFA.B3R5
17. Drift8
18. MCBXFAV.3R5/ MCBXFAH.3R5
19. Drift9 with Corrector package
20. MBXF.4R5
21. Drift10

Figure B.1: Scheme of the triplet on the right side of IP5.

Table B.1: IR5 triplet lattice elements included in the e-cloud simulations.

0.	Drift0	12.	MCBXFBV.B2R5
1.	MQXFA.A1R5		MCBXFBH.B2R5
2.	Drift1	13.	Drift6
3.	MQXFA.B1R5	14.	MQXFA.A3R5
4.	Drift2Q1	15.	Drift7
5.	Drift2Q2Q3	16.	MQXFA.B3R5
6.	MCBXFBV.A2R5	17.	Drift8
	MCBXFBH.A2R5	18.	MCBXFAV.3R5
7.	Drift3		MCBXFAH.3R5
8.	MQXFB.A2R5	19.	Drift9 with Corrector package
9.	Drift4	20.	MBXF.4R5
10.	MQXFB.B2R5	21.	Drift10
11.	Drift5		

Table B.2: Elements of the corrector package.

0.	MCTXF.3R5	4.	MCOXF.3R5
1.	MCTSXF.3R5	5.	MCOSXF.3R5
2.	MCDXF.3R5	6.	MCSXF.3R5
3.	MCDSXF.3R5	7.	MCSSXF.3R5

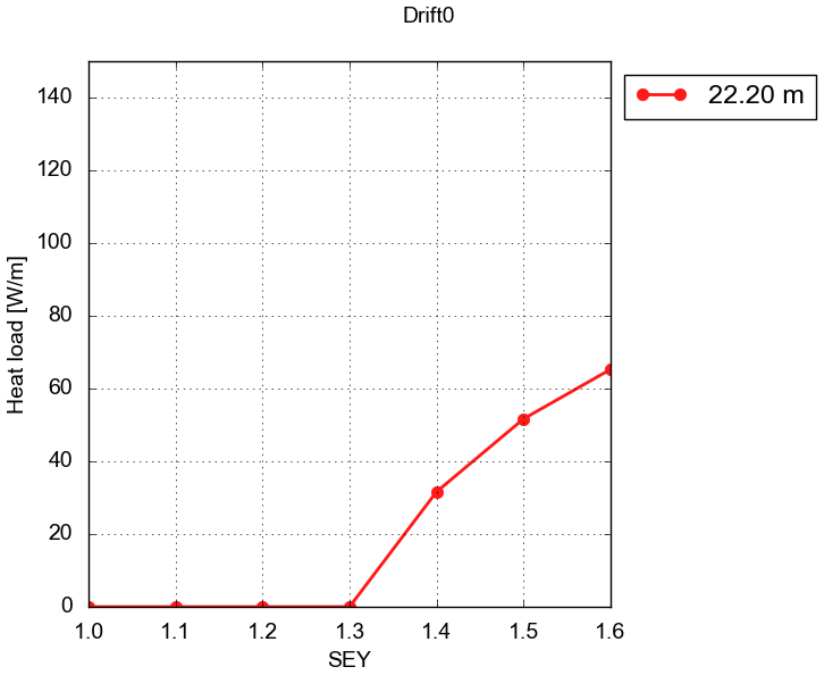

Figure B.2: Heat load as a function of the SEY at the simulated slices inside the Drift0.

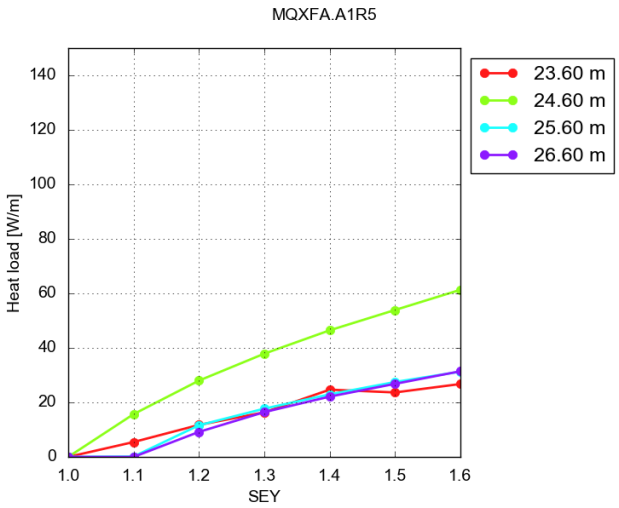

Figure B.3: Heat load as a function of the SEY at the simulated slices inside the MQXFA.A1R5 at its nominal strength.

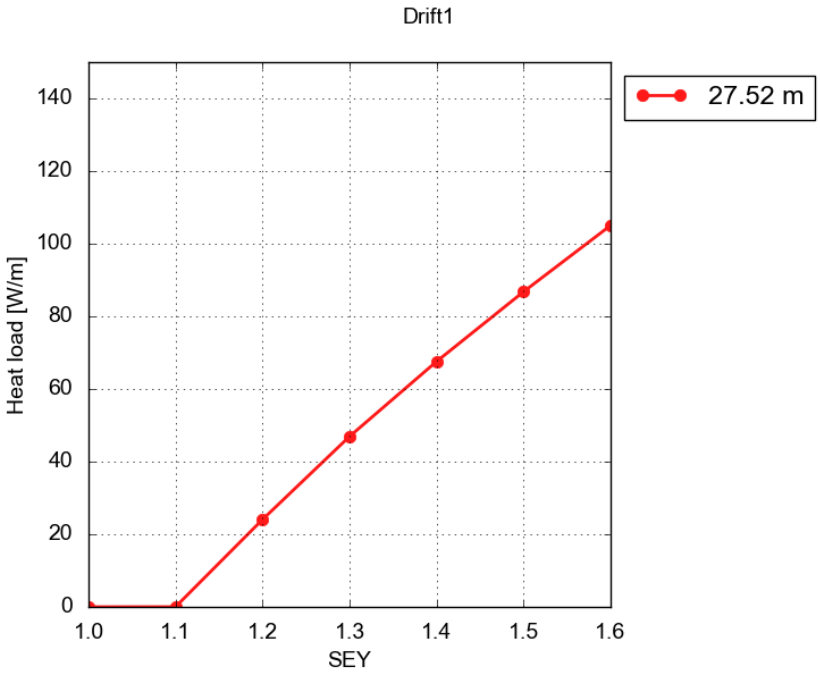

Figure B.4: Heat load as a function of the SEY at the simulated slices inside the Drift1.

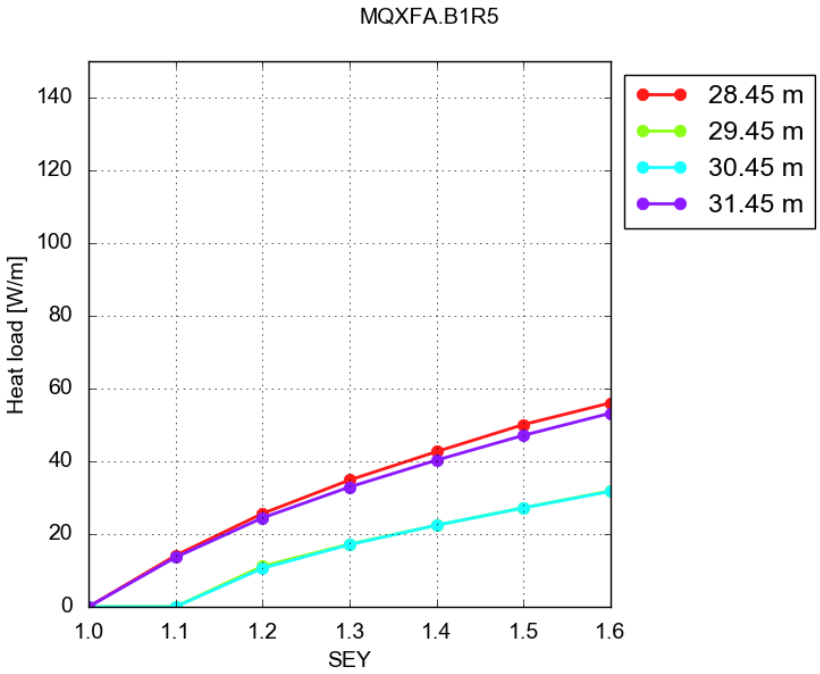

Figure B.5: Heat load as a function of the SEY at the simulated slices inside the MQXFA.B1R5 at its nominal strength.

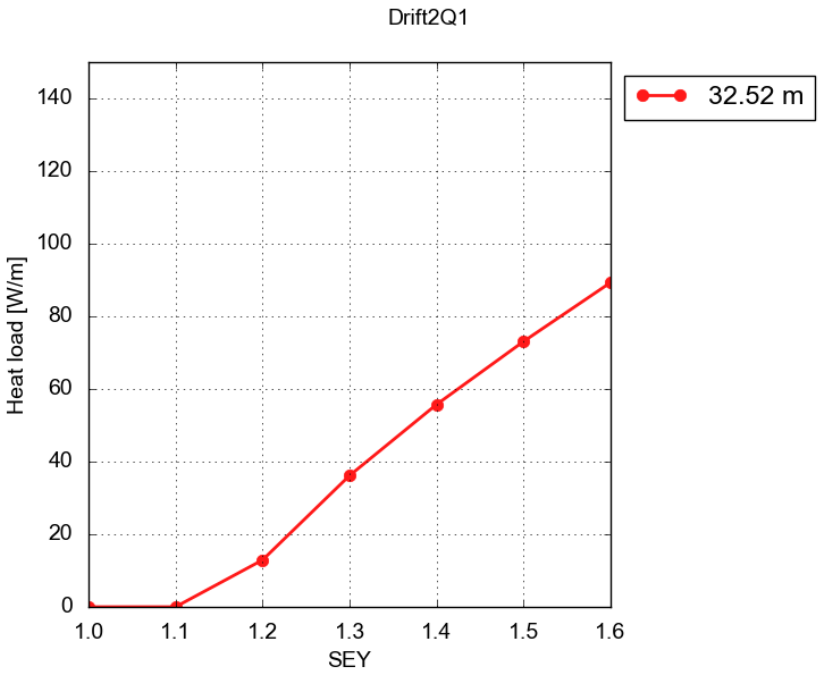

Figure B.6: Heat load as a function of the SEY at the simulated slices inside the Drift2Q1.

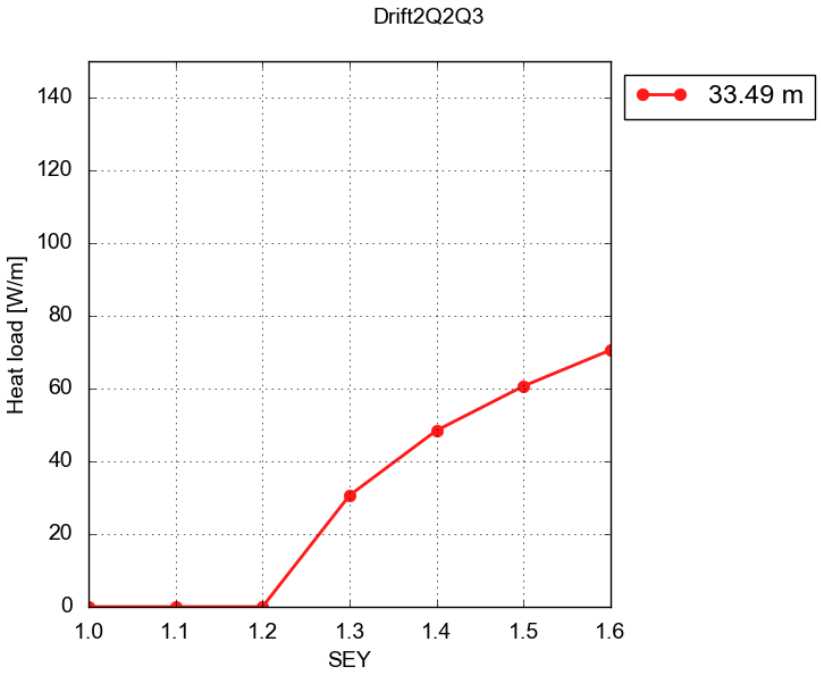

Figure B.7: Heat load as a function of the SEY at the simulated slices inside the Drift2Q2Q3.

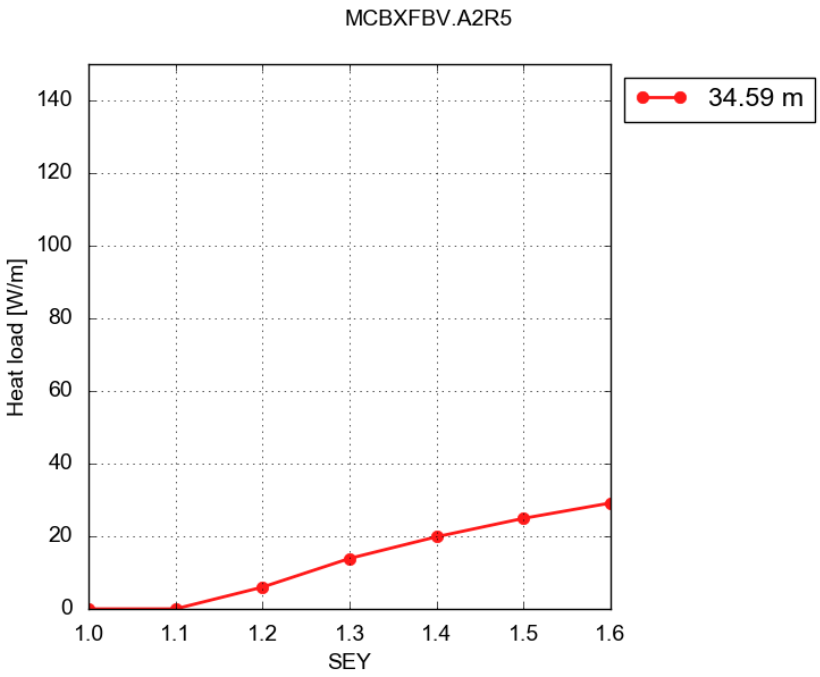

Figure B.8: Heat load as a function of the SEY at the simulated slices inside the MCBXFBV.A2R5 and MCBXFBH.A2R5 at their nominal strength.

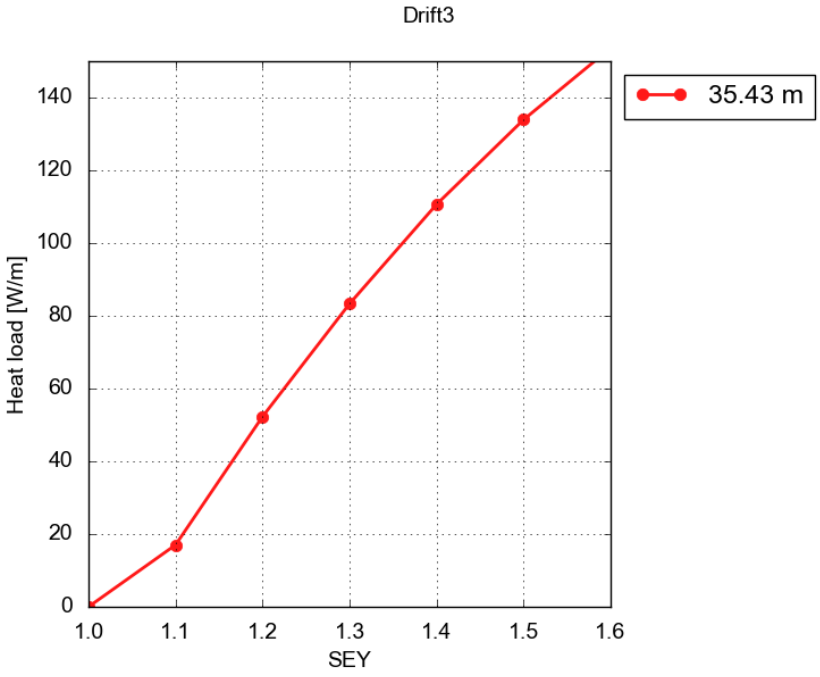

Figure B.9: Heat load as a function of the SEY at the simulated slices inside the Drift3.

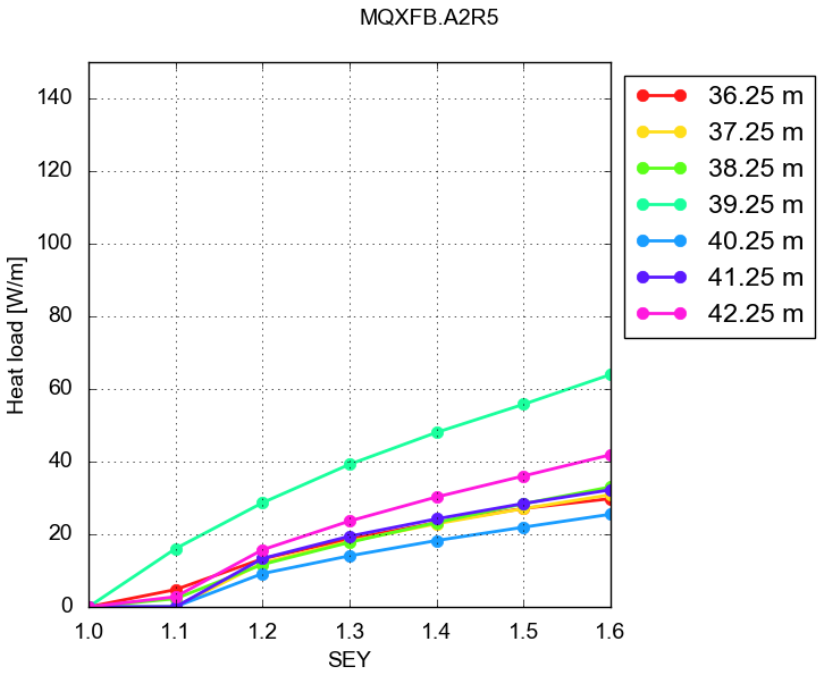

Figure B.10: Heat load as a function of the SEY at the simulated slices inside the MQXFB.A2R5 at its nominal strength.

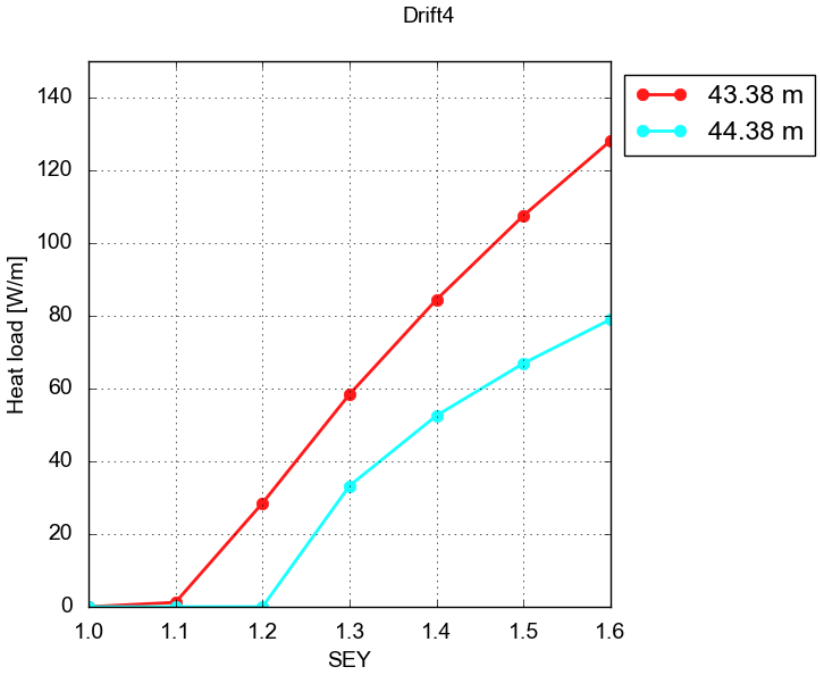

Figure B.11: Heat load as a function of the SEY at the simulated slices inside the Drift4.

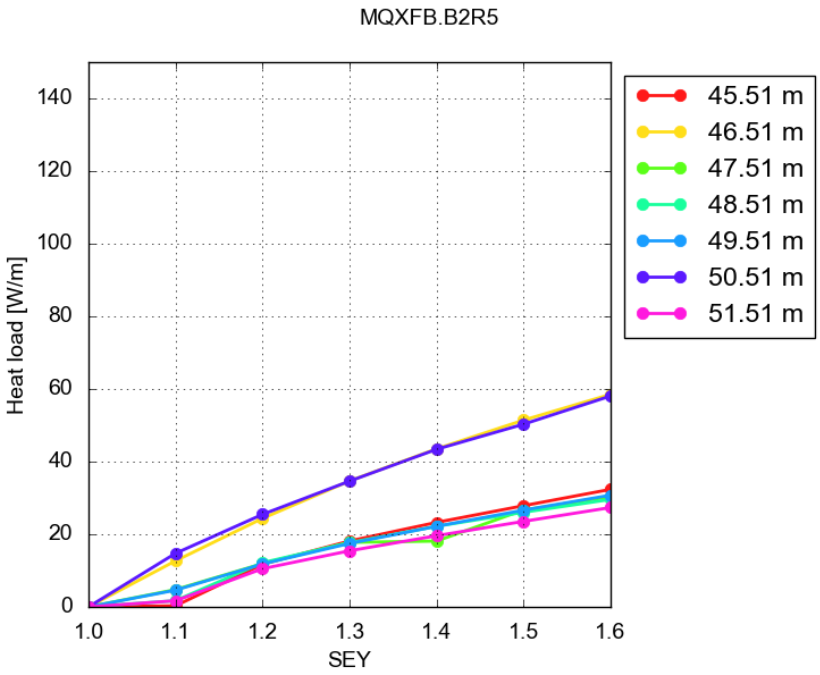

Figure B.12: Heat load as a function of the SEY at the simulated slices inside the MQXFB.B2R5 at its nominal strength.

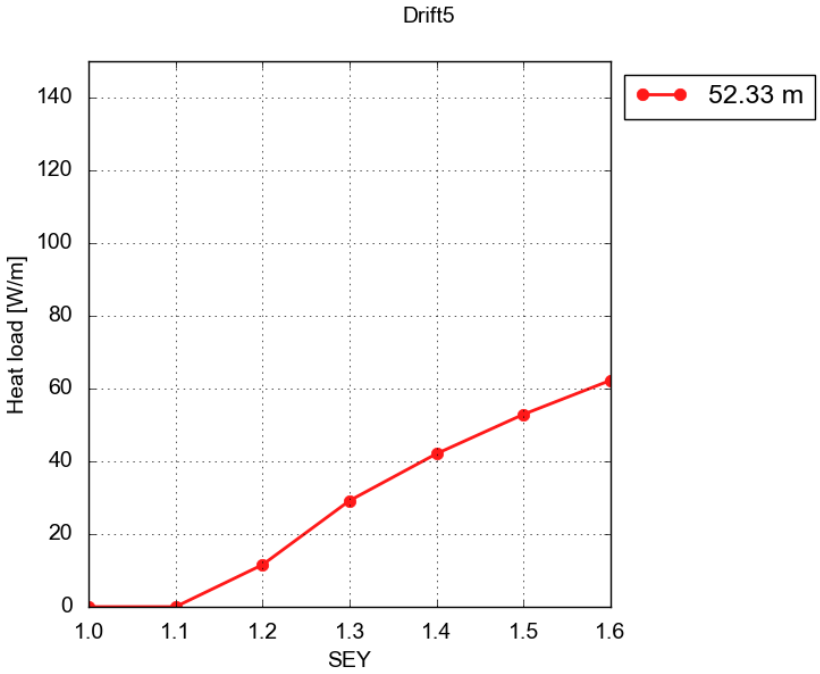

Figure B.13: Heat load as a function of the SEY at the simulated slices inside the Drift5.

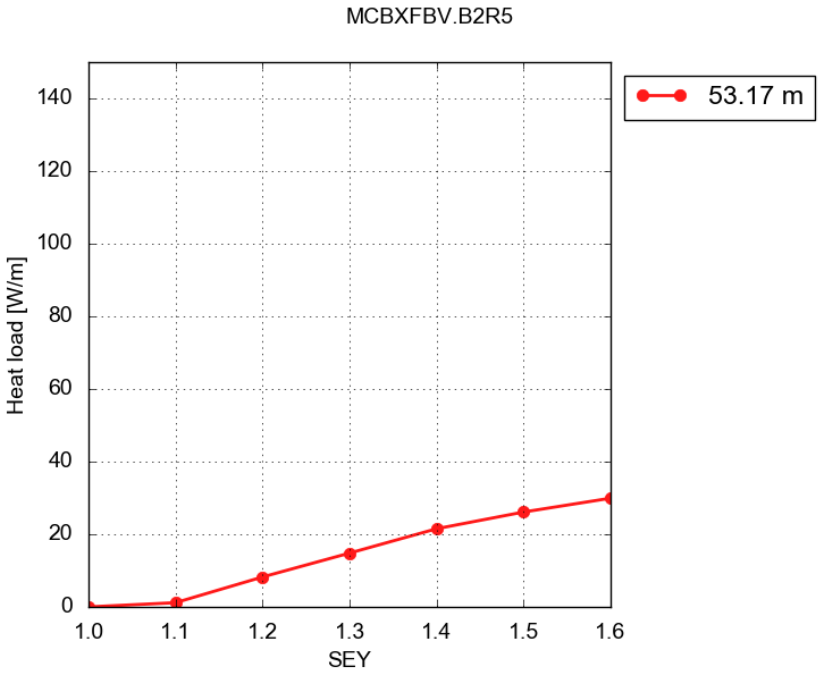

Figure B.14: Heat load as a function of the SEY at the simulated slices inside the MCBXFBV.B2R5 and MCBXFBH.B2R5 at their nominal strength.

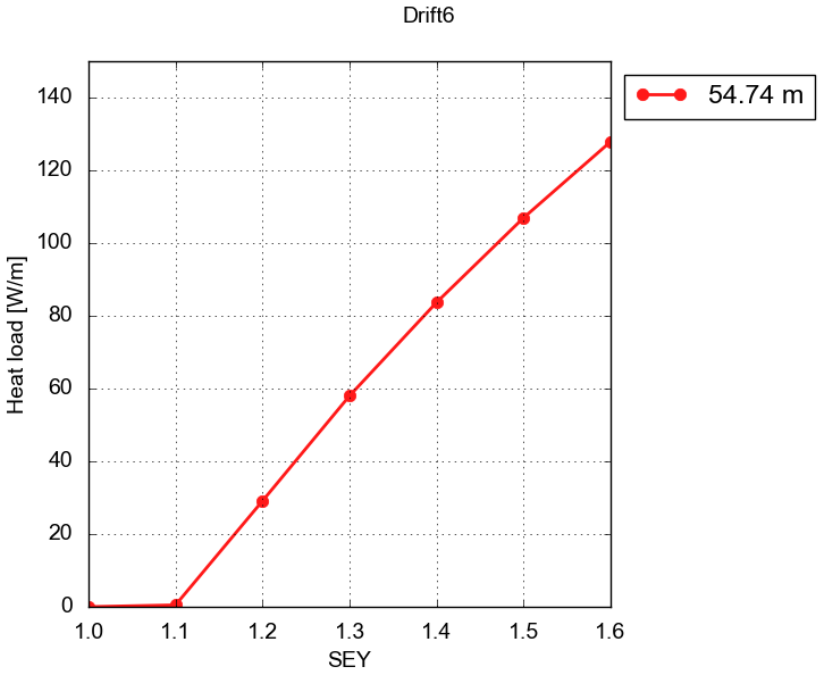

Figure B.15: Heat load as a function of the SEY at the simulated slices inside the Drift6.

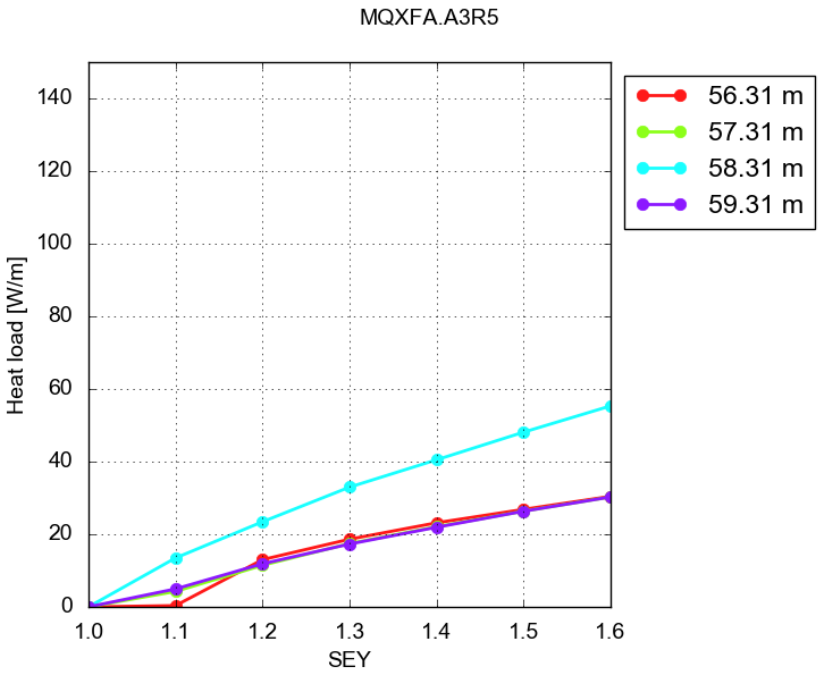

Figure B.16: Heat load as a function of the SEY at the simulated slices inside the MQXFA.A3R5 at its nominal strength.

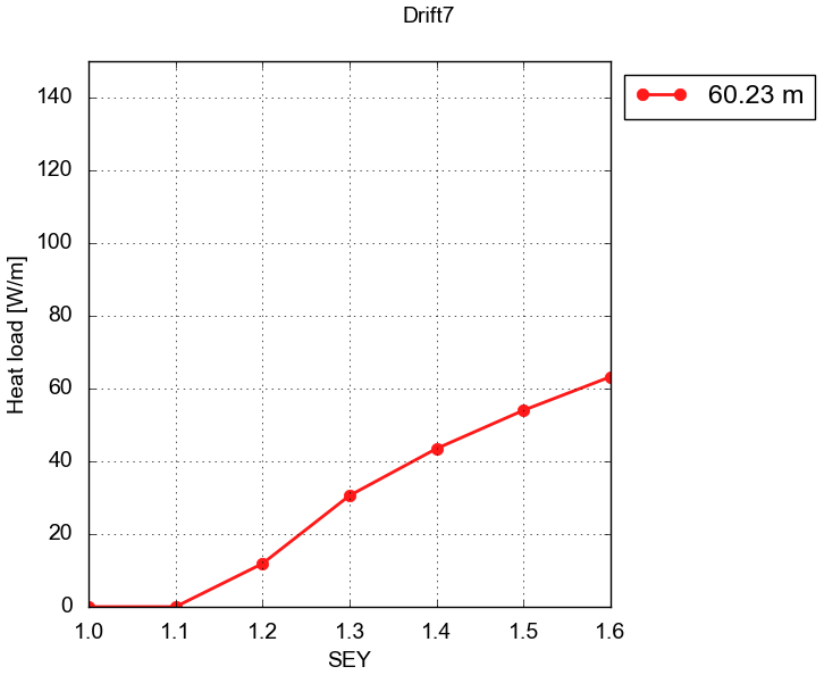

Figure B.17: Heat load as a function of the SEY at the simulated slices inside the Drift7.

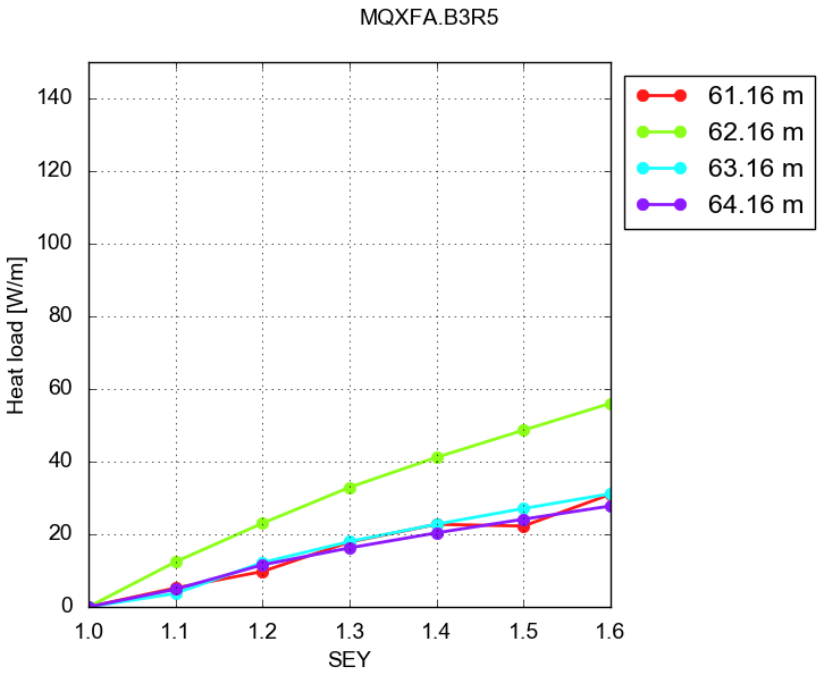

Figure B.18: Heat load as a function of the SEY at different slices inside the MQXFA.B3R5 at its nominal strength.

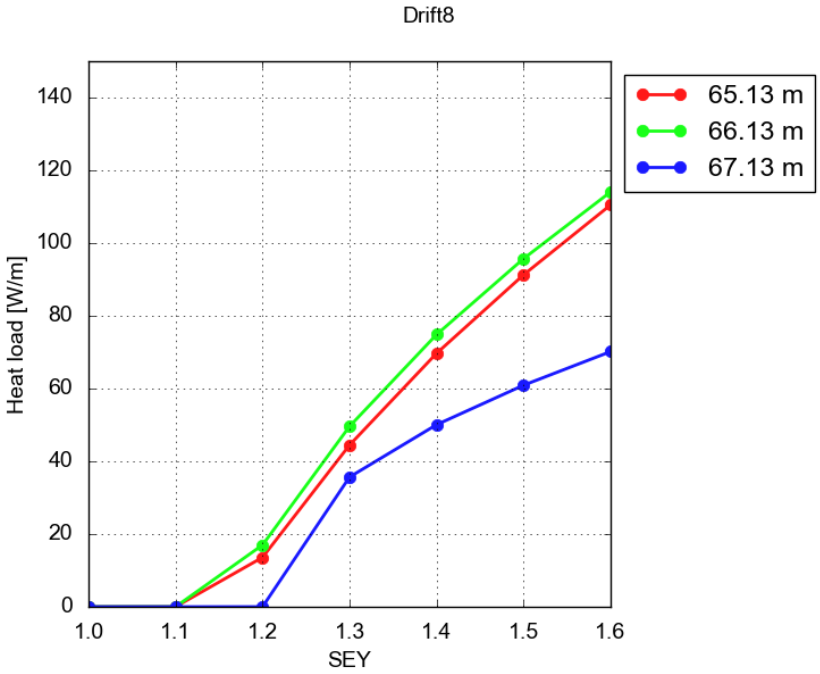

Figure B.19: Heat load as a function of the SEY at the simulated slices inside the Drift8.

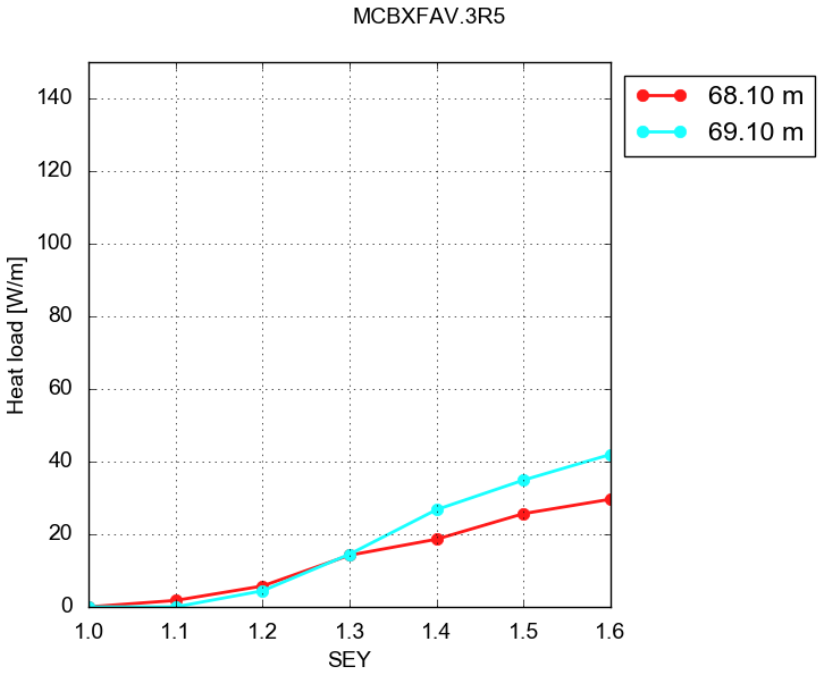

Figure B.20: Heat load as a function of the SEY at the simulated slices inside the MCBXFAV.3R5 and MCBXFAH.3R5 at their nominal strength.

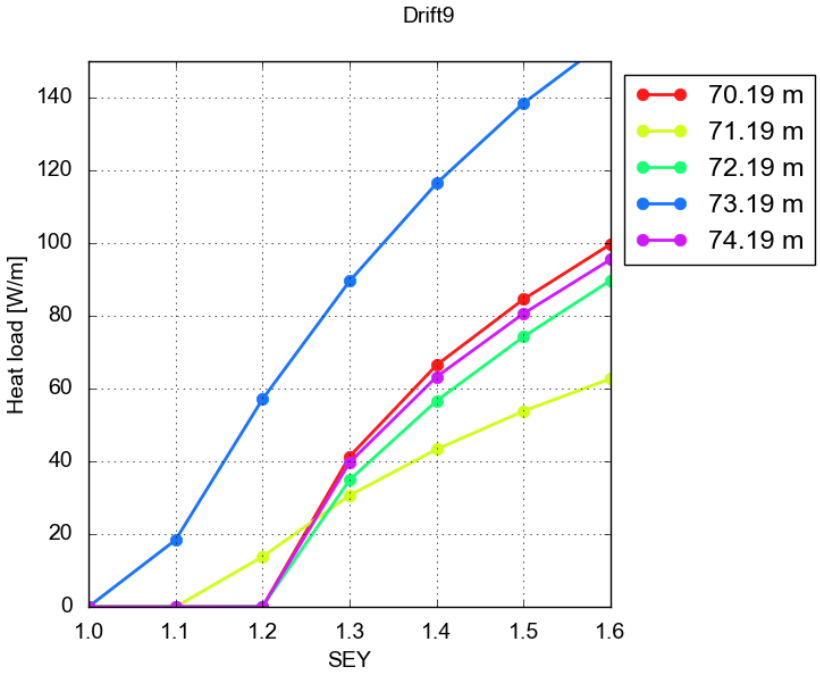

Figure B.21: Heat load as a function of the SEY at the simulated slices inside the Drift9.

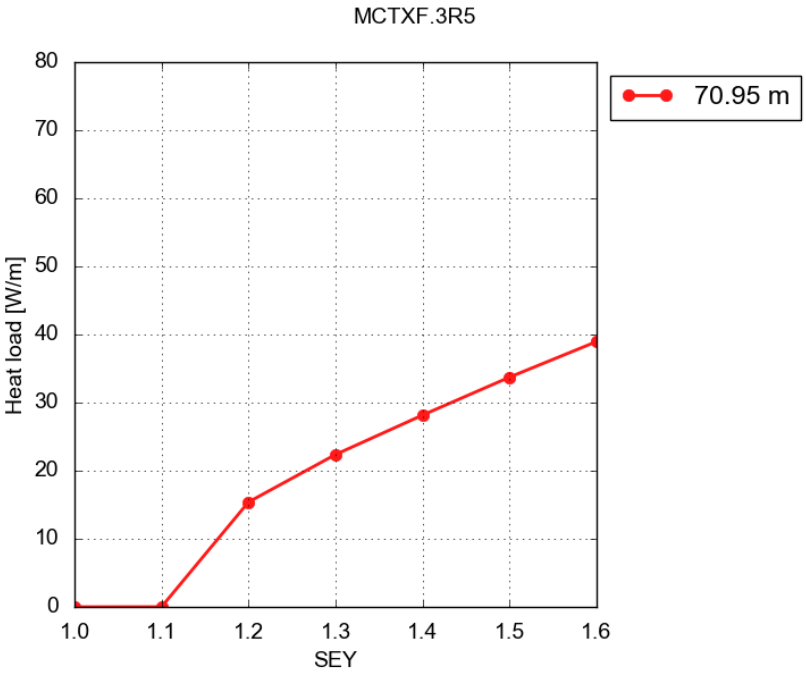

Figure B.22: Heat load as a function of the SEY at the simulated slices inside the MCTXF.3R5 dodecapole at its nominal strength.

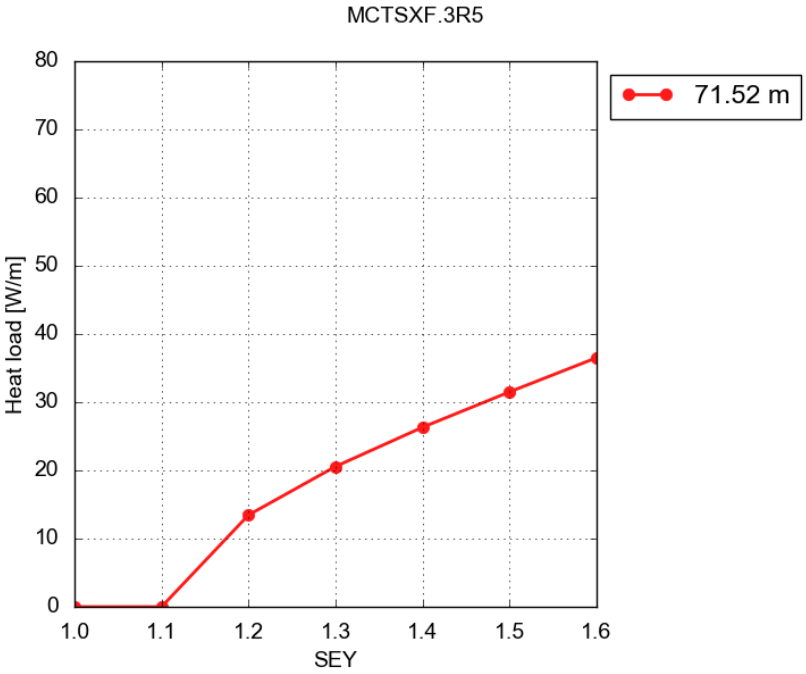

Figure B.23: Heat load as a function of the SEY at the simulated slices inside the MCTSXF.3R5 skew dodecapole at its nominal strength.

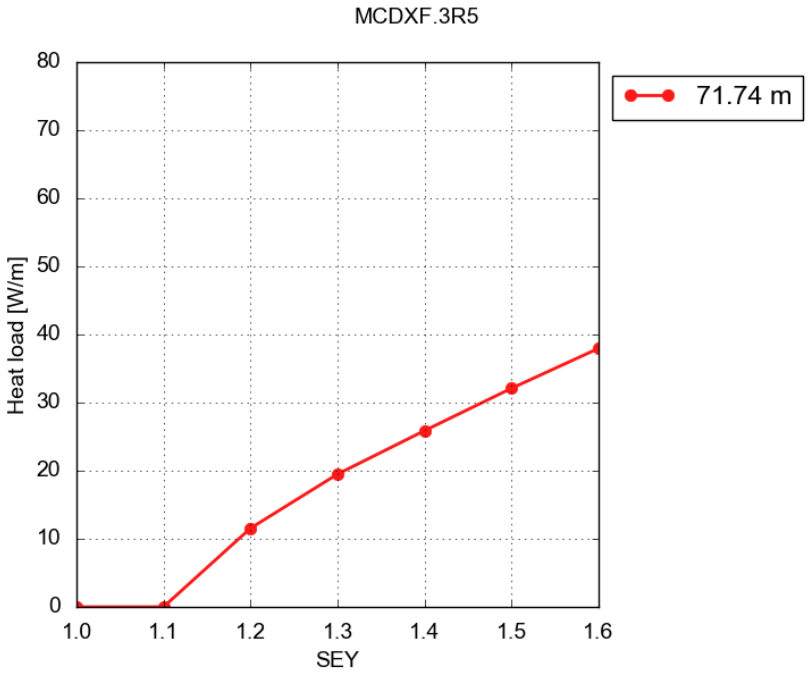

Figure B.24: Heat load as a function of the SEY at the simulated slices inside the MCDXF.3R5 decapole at its nominal strength.

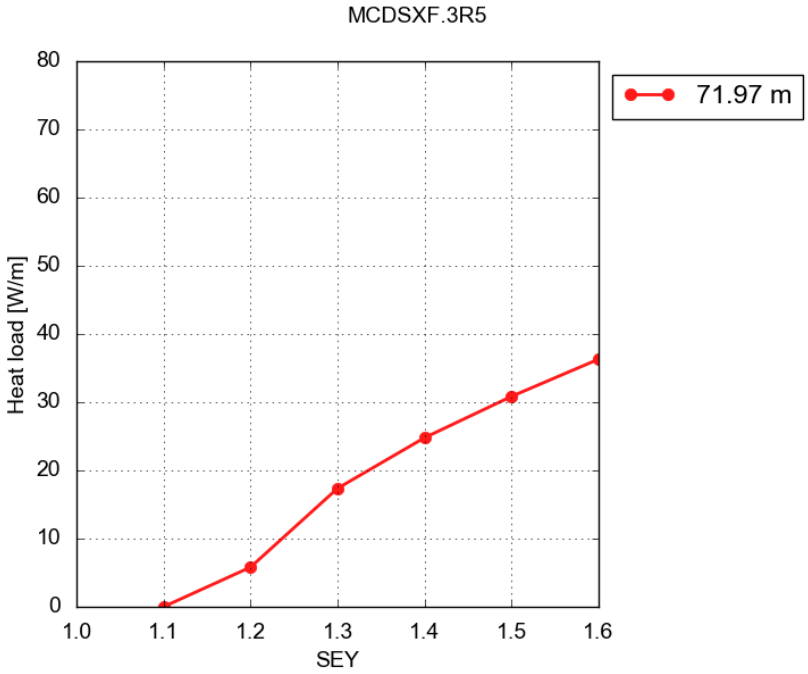

Figure B.25: Heat load as a function of the SEY at the simulated slices inside the MCDSXF.3R5 skew decapole at its nominal strength.

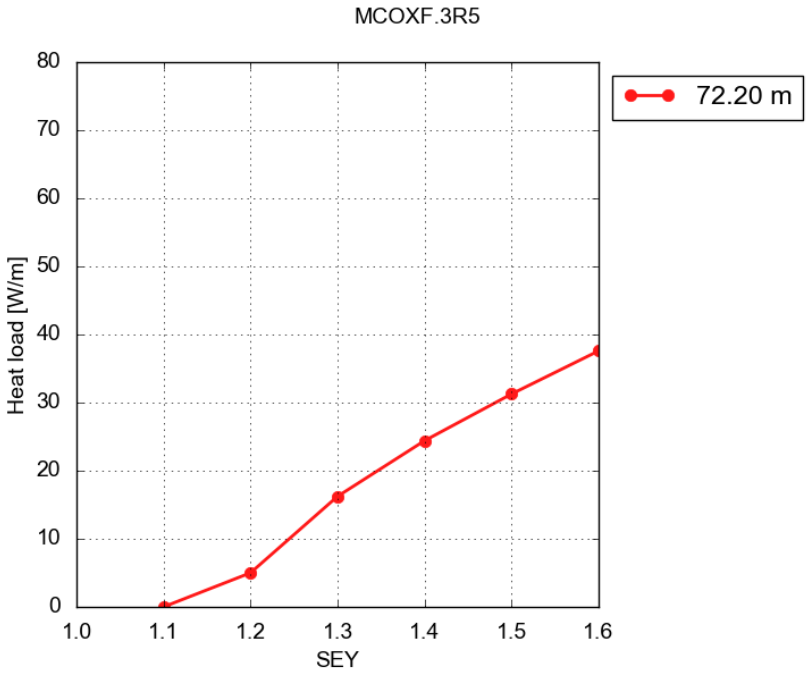

Figure B.26: Heat load as a function of the SEY at the simulated slices inside the MCOXF.3R5 octupole at its nominal strength.

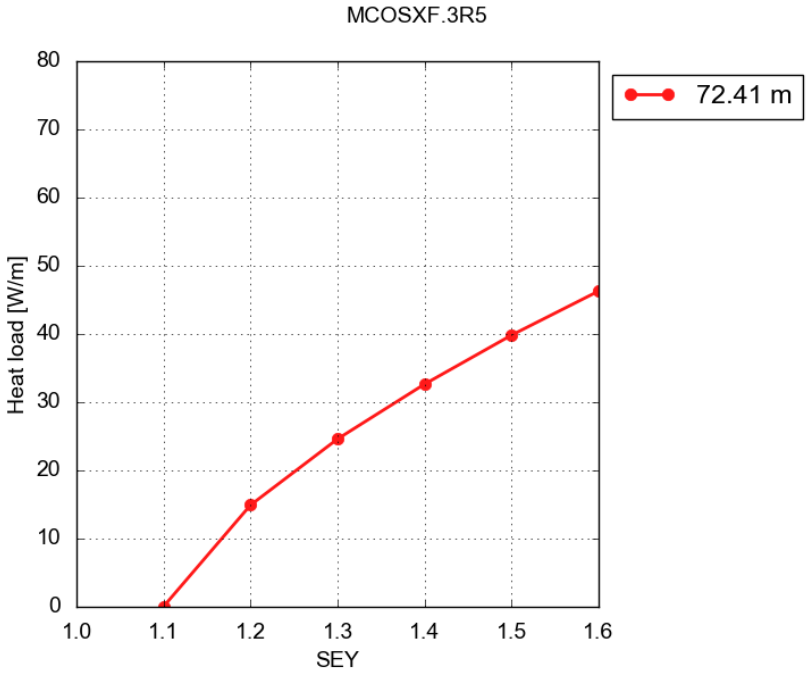

Figure B.27: Heat load as a function of the SEY at the simulated slices inside the MCOSXF.3R5 skew octupole at its nominal strength.

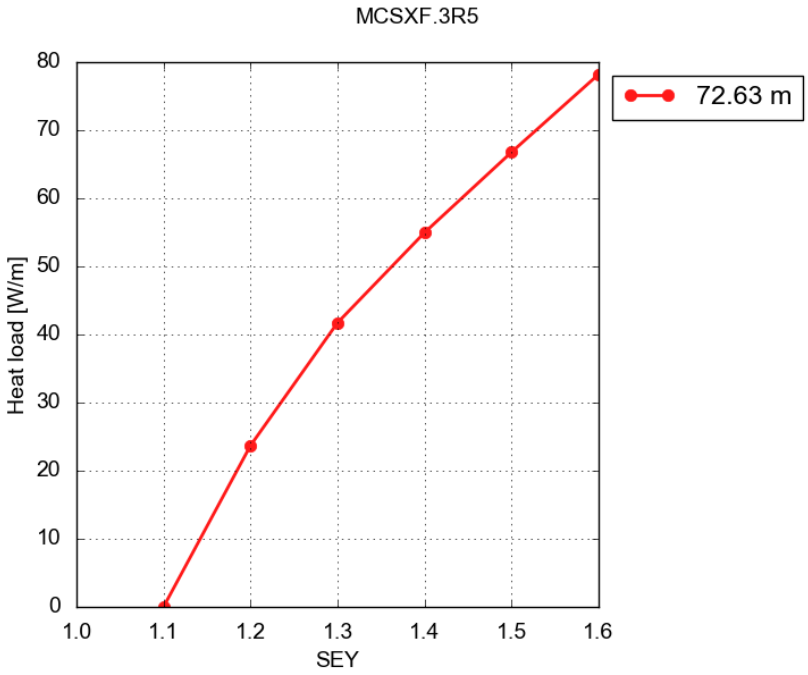

Figure B.28: Heat load as a function of the SEY at the simulated slices inside the MCSXF.3R5 sextupole at its nominal strength.

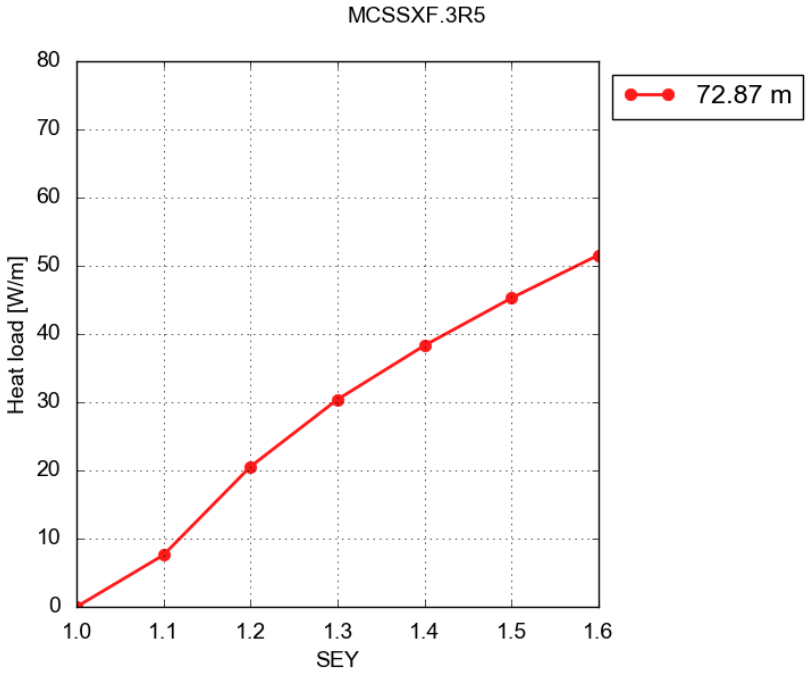

Figure B.29: Heat load as a function of the SEY at the simulated slices inside the MCSSXF.3R5 skew sextupole at its nominal strength.

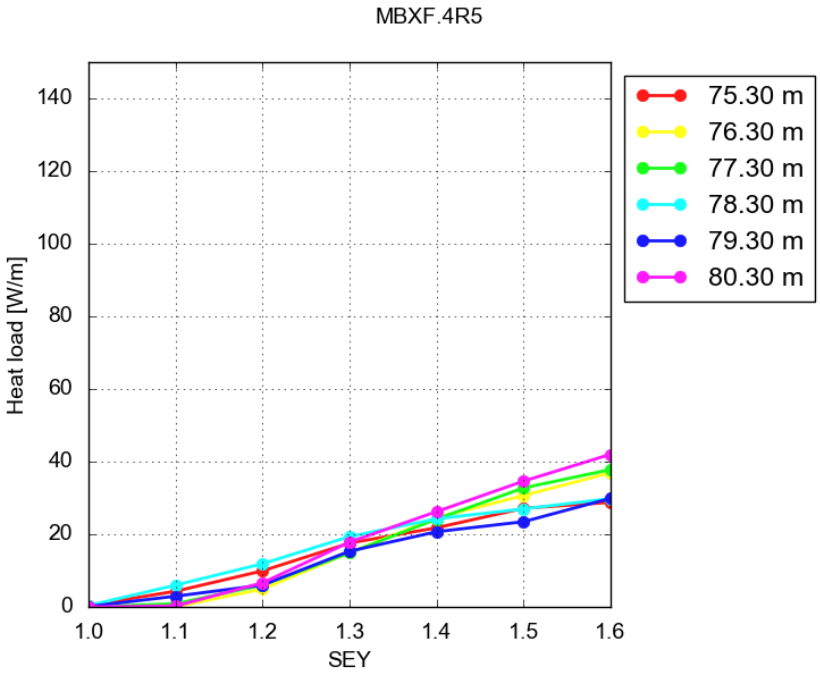

Figure B.30: Heat load as a function of the SEY at the simulated slices inside the MBXF.4R5 at its nominal strength.

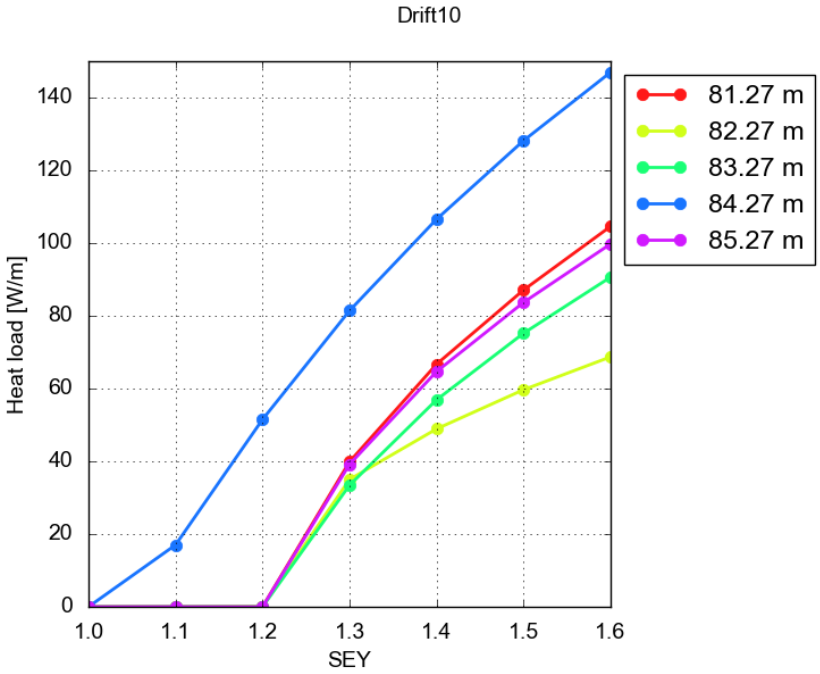

Figure B.31: Heat load as a function of the SEY at the simulated slices inside the Drift10.

Appendix C

Heat load vs SEY for all simulated sections of the triplets in IR2 and IR8

In the following we report the heat load as a function of the SEY for all simulated sections of the triplet in IR8 (same in IR2). A schematic layout of the triplet is displayed in Fig C.1. The different elements are numbered and the corresponding names are reported in Tab. C.1. The simulated sections are marked by vertical black lines. The vertical blue lines indicate the locations where a change in the beam screen geometry takes place.

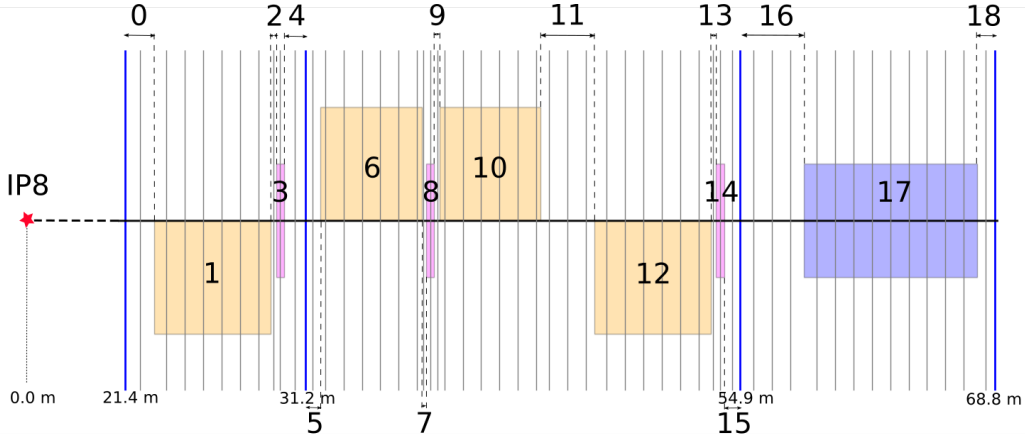

Figure C.1: Scheme of the triplet on the right side of IP8.

Table C.1: IR8 triplet lattice elements included in the e-cloud simulations.

0.	Drift0	9.	Drift4
1.	MQXA.1R8	10.	MQXB.B2R8
2.	Drift1	11.	Drift5
3.	MCBXV.1R8	12.	MQXA.3R8
	MCBXH.1R8	13.	Drift6
4.	Drift2Q1	14.	MCBXV.3R8
5.	Drift2Q2Q3		MCBXH.3R8
6.	MQXB.A2R8	15.	Drift7Q2Q3
7.	Drift3	16.	Drift7D1
8.	MCBXV.2R8	17.	MBX.4R8
	MCBXH.2R8	18.	Drift8

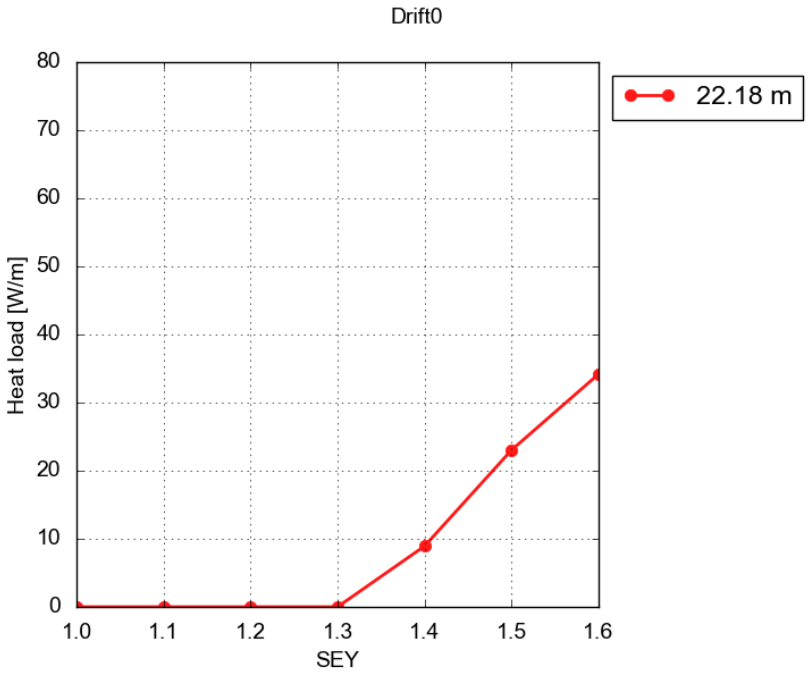

Figure C.2: Heat load as a function of the SEY at the simulated slices inside the Drift0.

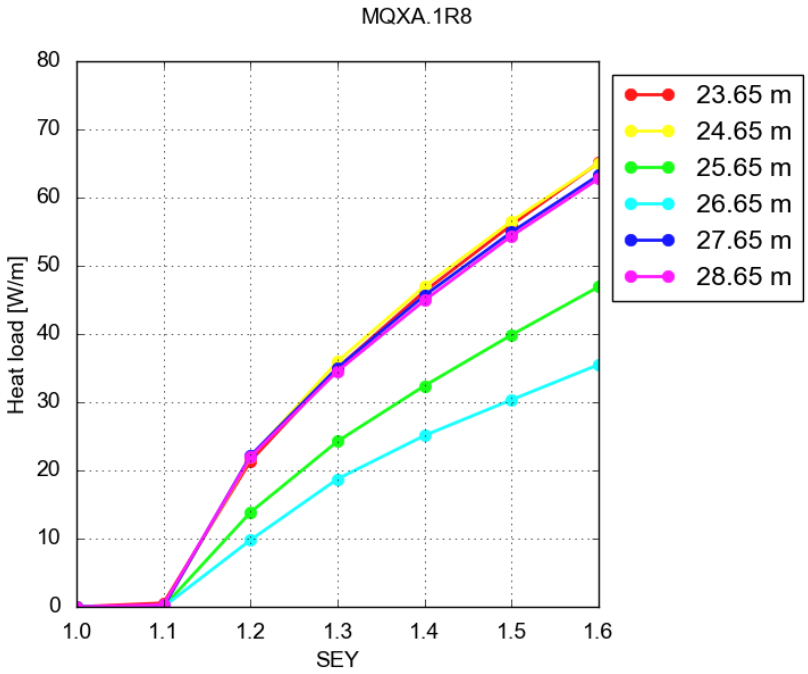

Figure C.3: Heat load as a function of the SEY at the simulated slices inside the MQXA.1R8 at its nominal strength.

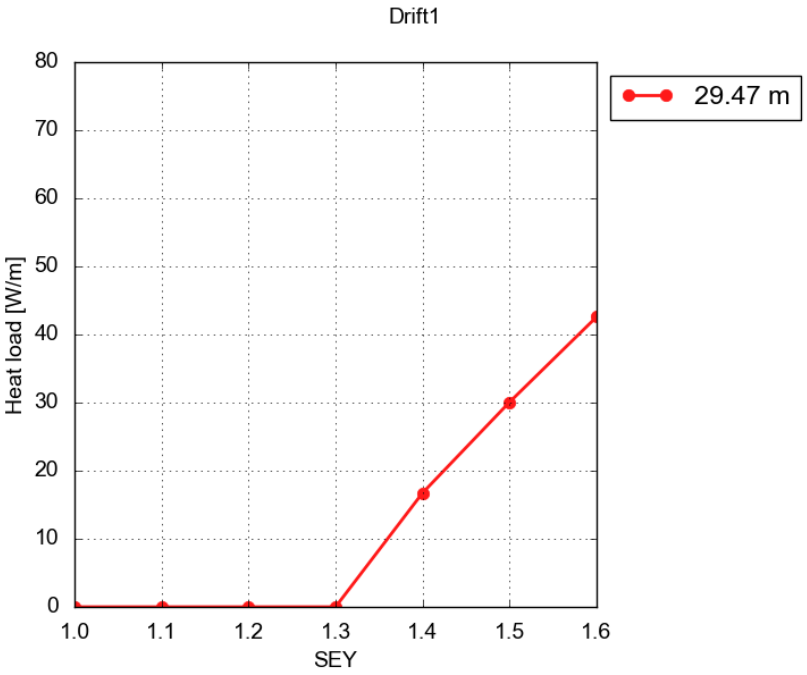

Figure C.4: Heat load as a function of the SEY at the simulated slices inside the Drift1.

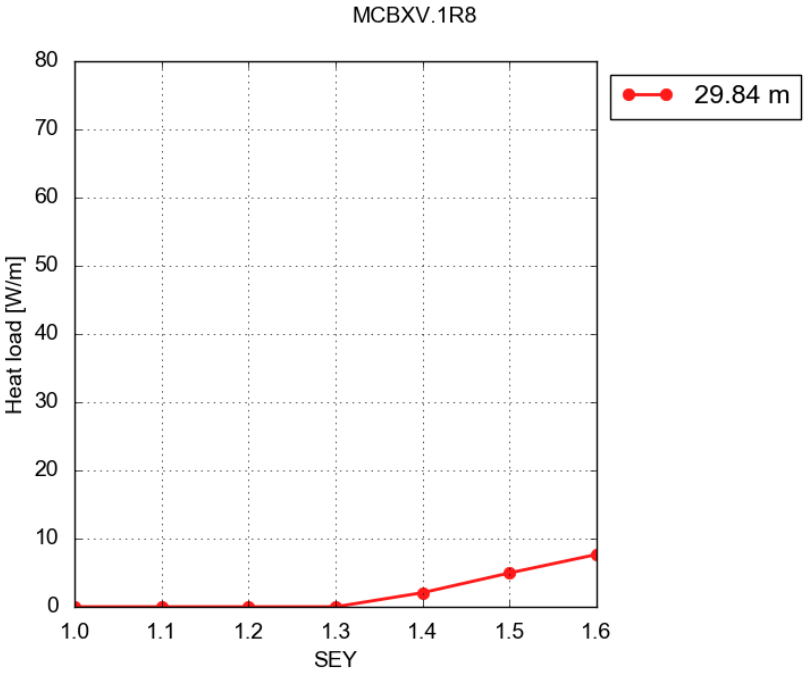

Figure C.5: Heat load as a function of the SEY at the simulated slices inside the MCBXV.1R8 and MCBXH.1R8 at their nominal strength.

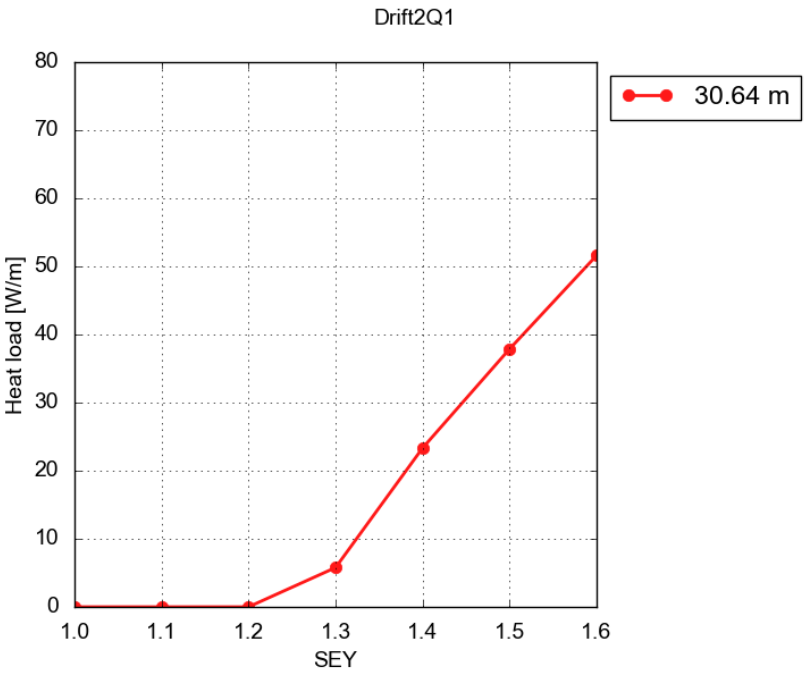

Figure C.6: Heat load as a function of the SEY at the simulated slices inside the Drift2Q1.

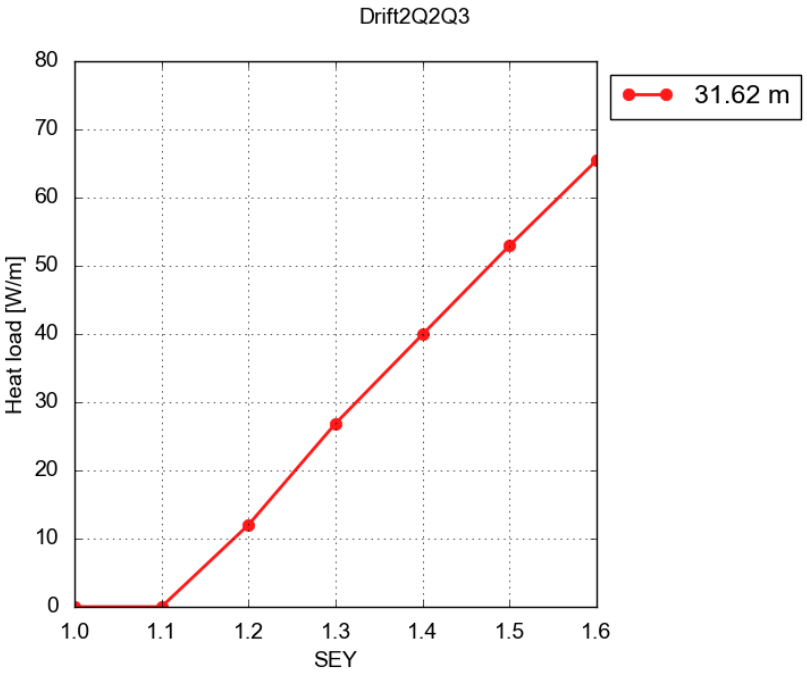

Figure C.7: Heat load as a function of the SEY at the simulated slices inside the Drift2Q2Q3.

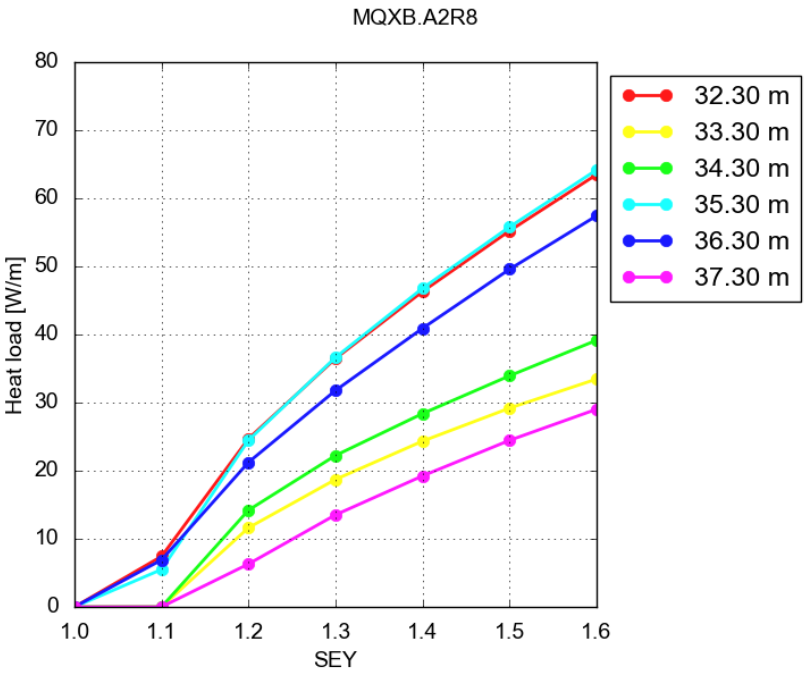

Figure C.8: Heat load as a function of the SEY at the simulated slices inside the MQXB.A2R8 at its nominal strength.

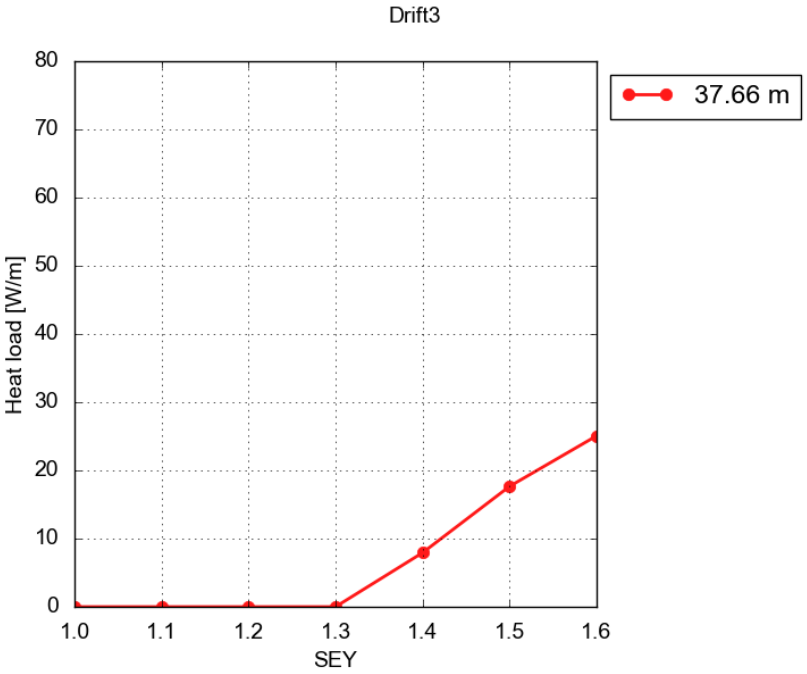

Figure C.9: Heat load as a function of the SEY at the simulated slices inside the Drift3.

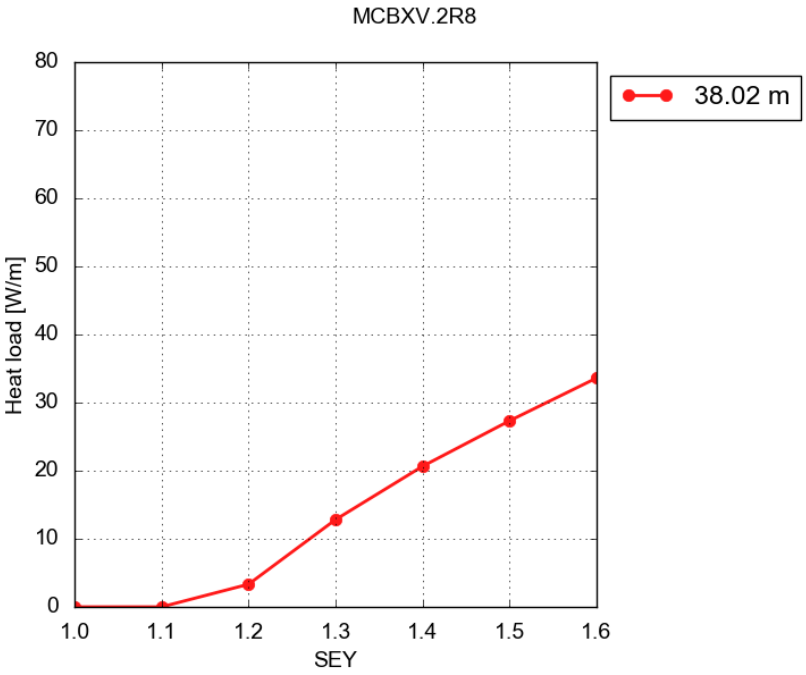

Figure C.10: Heat load as a function of the SEY at the simulated slices inside the MCBXV.2R8 and MCBXH.2R8 at their nominal strength.

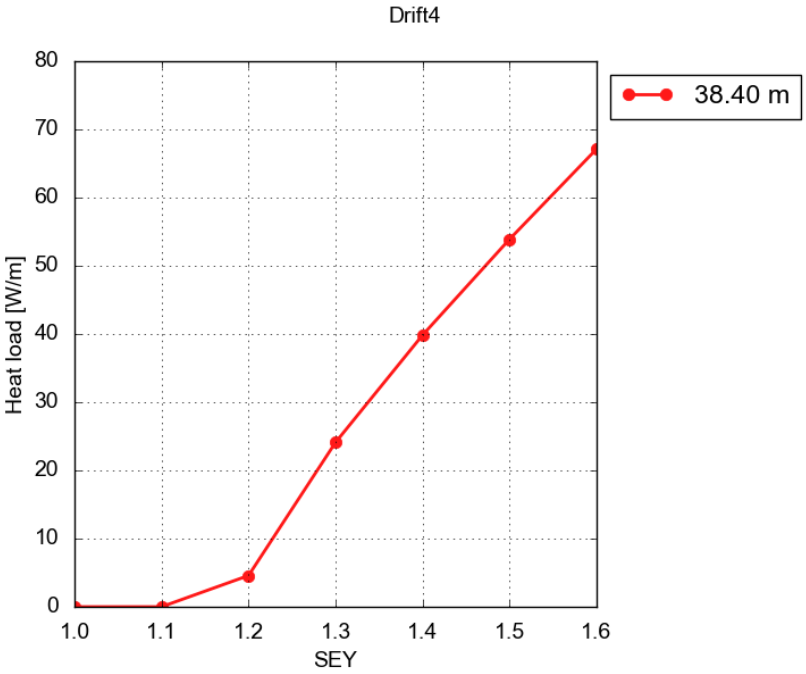

Figure C.11: Heat load as a function of the SEY at the simulated slices inside the Drift4.

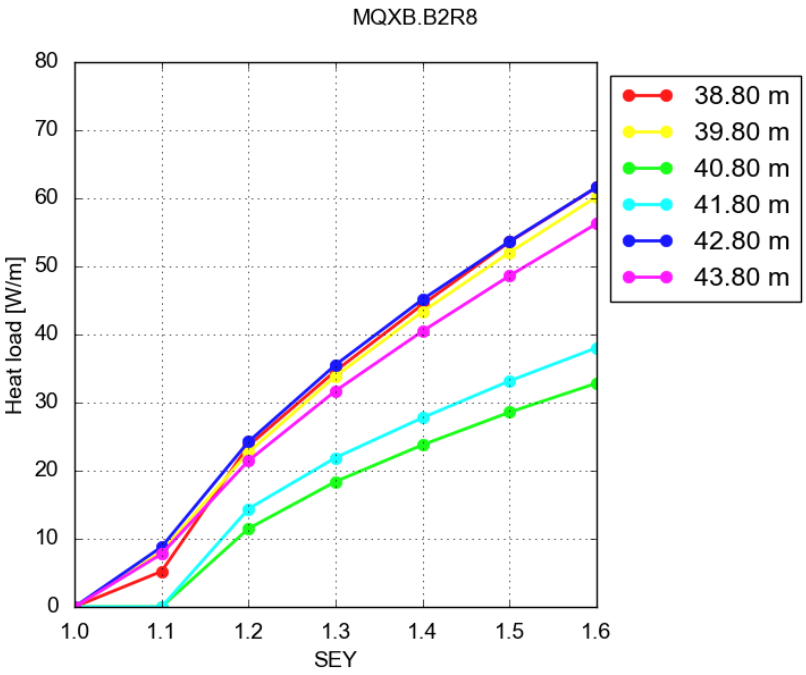

Figure C.12: Heat load as a function of the SEY at the simulated slices inside the MQXB.B2R8 at its nominal strength.

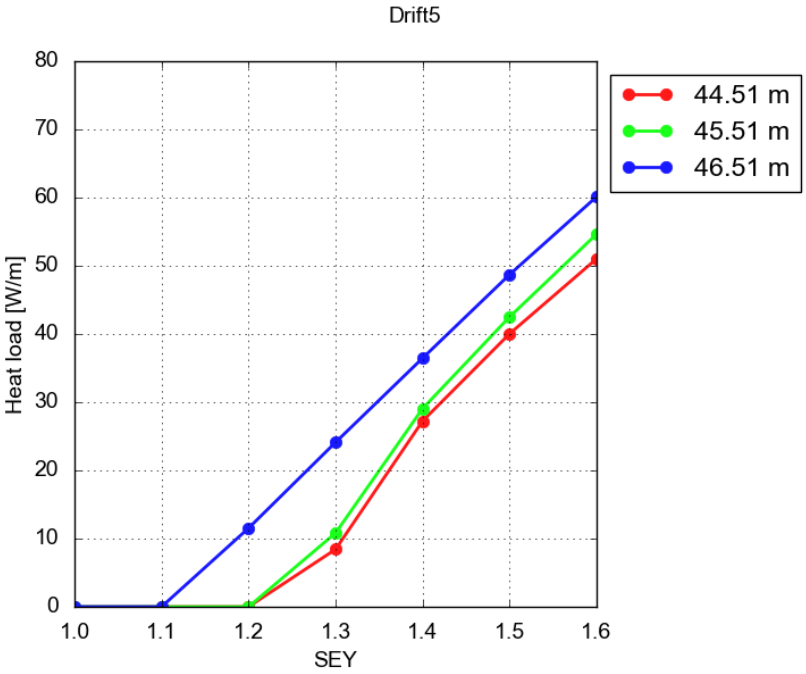

Figure C.13: Heat load as a function of the SEY at the simulated slices inside the Drift5.

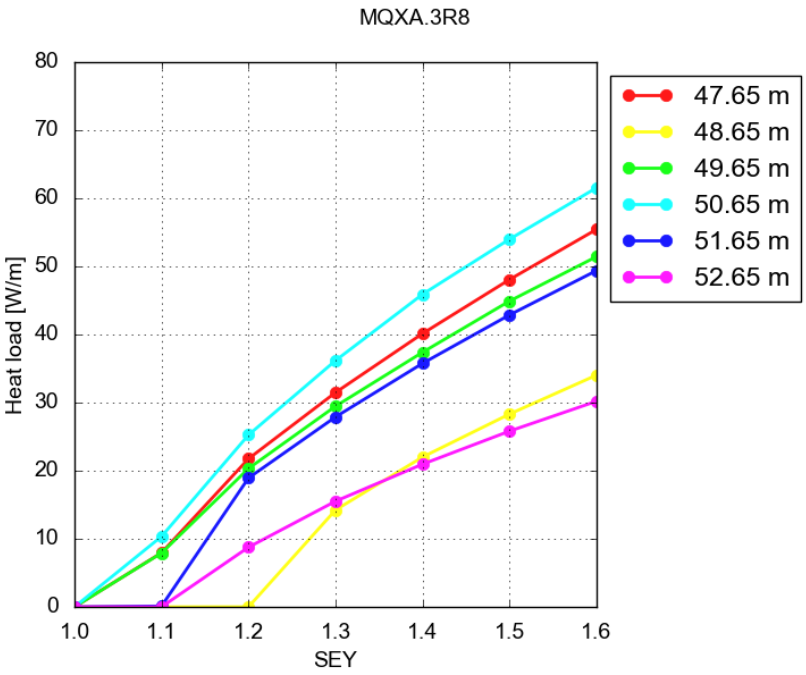

Figure C.14: Heat load as a function of the SEY at the simulated slices inside the MQXA.3R8 at its nominal strength.

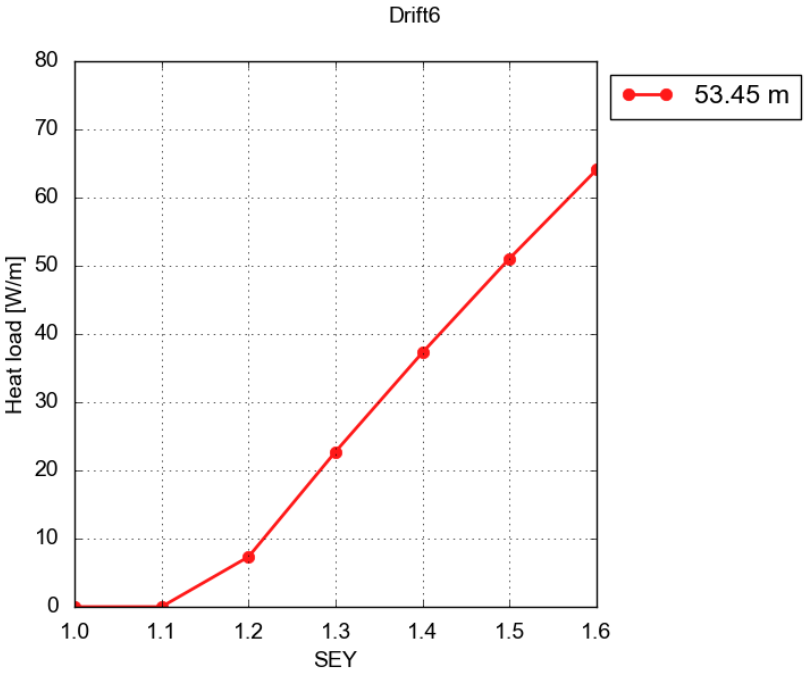

Figure C.15: Heat load as a function of the SEY at the simulated slices inside the Drift6.

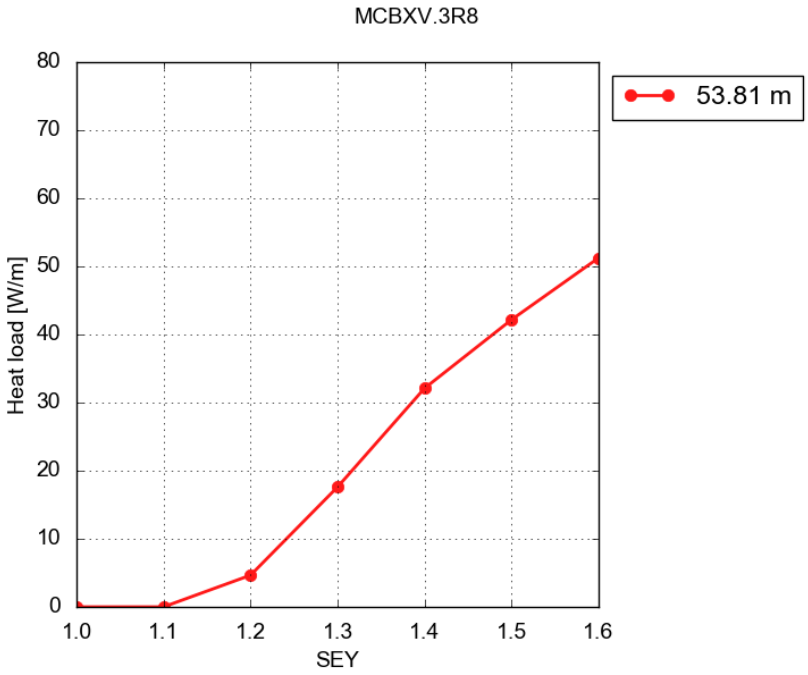

Figure C.16: Heat load as a function of the SEY at the simulated slices inside the MCBXV.3R8 and MCBXH.3R8 at its nominal strength.

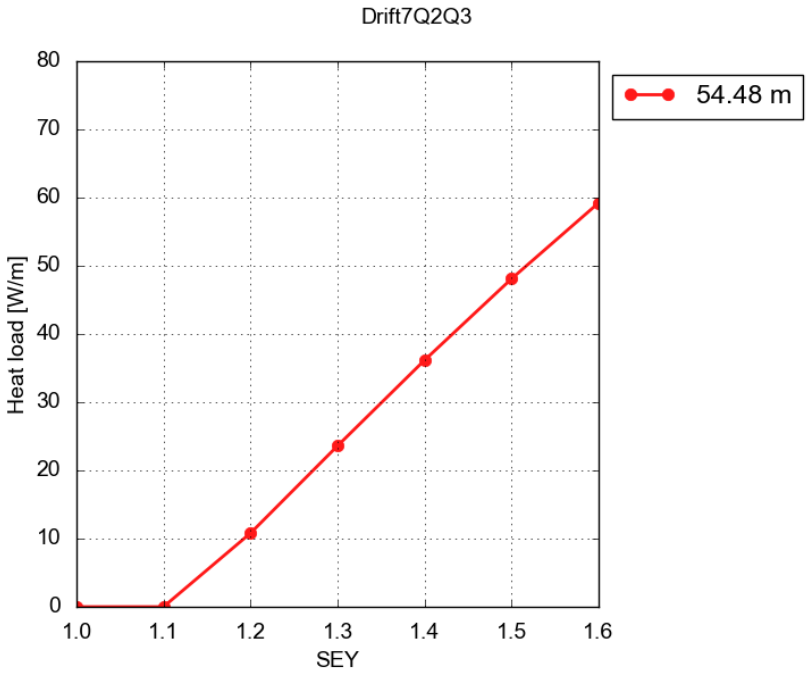

Figure C.17: Heat load as a function of the SEY at the simulated slices inside the Drift7Q2Q3.

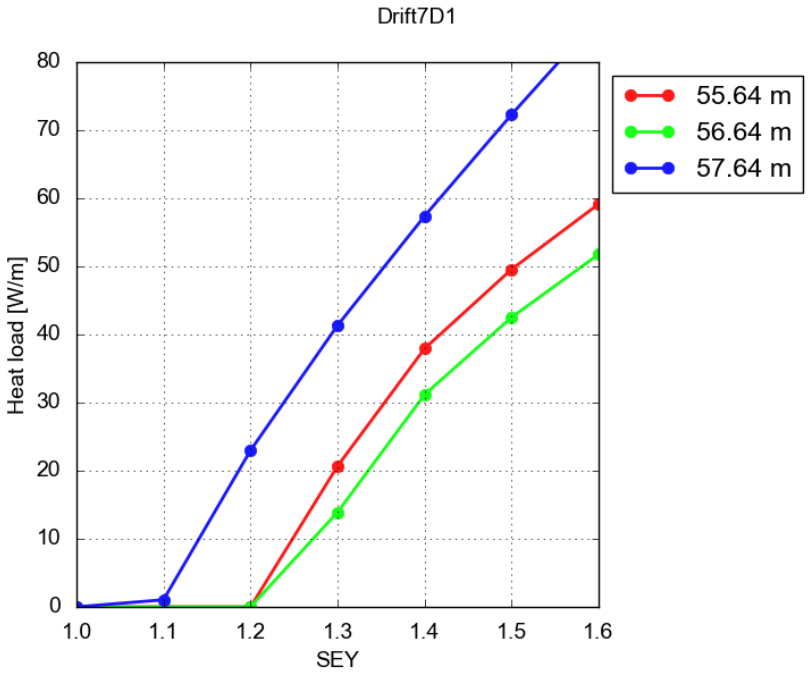

Figure C.18: Heat load as a function of the SEY at the simulated slices inside the Drift7D1.

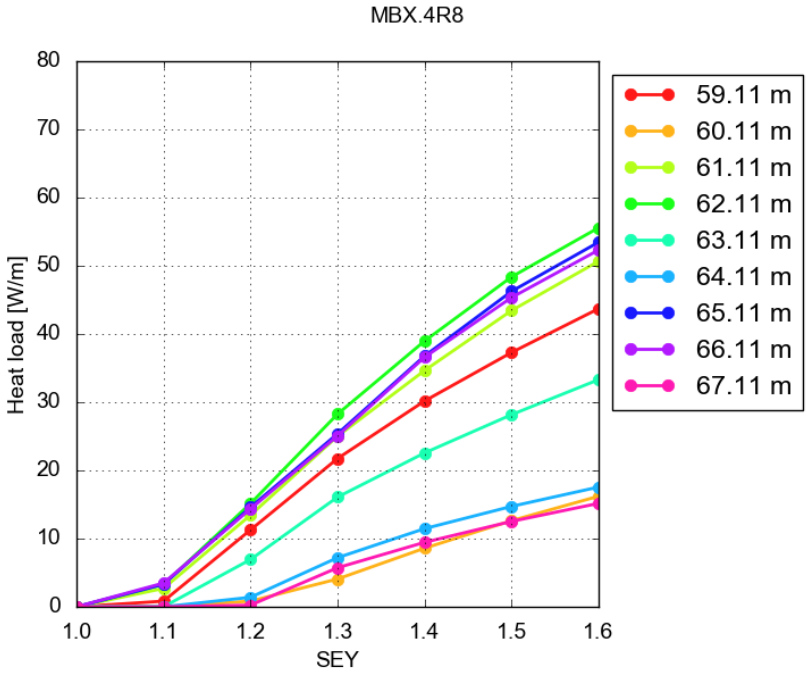

Figure C.19: Heat load as a function of the SEY at the simulated slices inside the MBX.4R8 at its nominal strength.

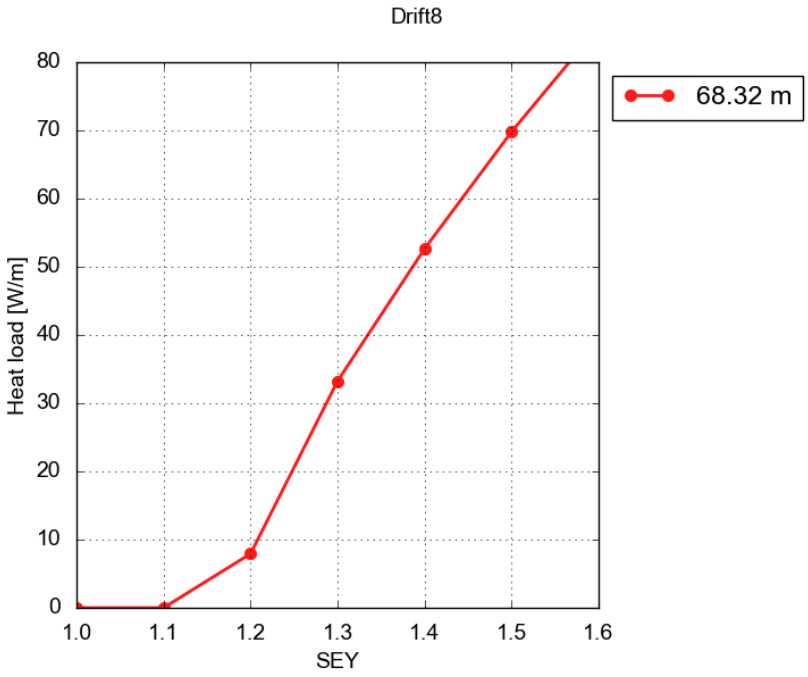

Figure C.20: Heat load as a function of the SEY at the simulated slices inside the Drift8.

Appendix D

Heat load tables for uniform SEY

Name	Length	Field config.	Chamber	Impedance (T_BS=70 K)	e-cloud (SEY=1.1)	Total
ITQ1R5	11.6 m		BSHL_Q1	4.1 W	51.5 W	55.5 W
MQXFA.A1R5	4.2 m	quad	BSHL_Q1	1.5 W	22.3 W	
MQXFA.B1R5	4.2 m	quad	BSHL_Q1	1.5 W	29.1 W	
Drifts	3.2 m	drift	BSHL_Q1	1.1 W	0.0 W	
ITQ2Q3R5	49.1 m		BSHL_Q23	15.3 W	166.7 W	182.0 W
MQXFB.A2R5	7.2 m	quad	BSHL_Q23	2.3 W	26.5 W	
MQXFB.B2R5	7.2 m	quad	BSHL_Q23	2.3 W	41.4 W	
MQXFA.A3R5	4.2 m	quad	BSHL_Q23	1.3 W	24.2 W	
MQXFA.B3R5	4.2 m	quad	BSHL_Q23	1.3 W	27.5 W	
MBXF.4R5	6.3 m	dip	BSHL_Q23	2.0 W	15.1 W	
MCBXFBV.A2R5	1.2 m	dip	BSHL_Q23	0.4 W	0.0 W	
MCBXFBH.A2R5						
MCBXFBV.B2R5	1.2 m	dip	BSHL_Q23	0.4 W	1.4 W	
MCBXFBH.B2R5						
MCBXFAV.3R5	2.2 m	dip	BSHL_Q23	0.7 W	2.0 W	
MCBXFAH.3R5						
Drifts	15.6 m	drift	BSHL_Q23	4.7 W	28.8 W	
Total IT R5						**237.6 W**

Table D.1: Expected heat loads for the different elements of the inner triplet on the right side of IP5. The electron cloud contribution is evaluated for SEY=1.1.

Name	Length	Field config.	Chamber	Impedance (T_BS=70 K)	e-cloud (SEY=1.3)	Total
ITQ1R5	11.6 m		BSHL_Q1	4.1 W	264.8 W	268.9 W
MQXFA.A1R5	4.2 m	quad	BSHL_Q1	1.5 W	92.8 W	
MQXFA.B1R5	4.2 m	quad	BSHL_Q1	1.5 W	107.2 W	
Drifts	3.2 m	drift	BSHL_Q1	1.1 W	64.8 W	
ITQ2Q3R5	49.1 m		BSHL_Q23	15.3 W	1378.5 W	1393.8 W
MQXFB.A2R5	7.2 m	quad	BSHL_Q23	2.3 W	154.2 W	
MQXFB.B2R5	7.2 m	quad	BSHL_Q23	2.3 W	159.2 W	
MQXFA.A3R5	4.2 m	quad	BSHL_Q23	1.3 W	90.7 W	
MQXFA.B3R5	4.2 m	quad	BSHL_Q23	1.3 W	89.3 W	
MBXF.4R5	6.3 m	dip	BSHL_Q23	2.0 W	104.4 W	
MCBXFBV.A2R5	1.2 m	dip	BSHL_Q23	0.4 W	16.7 W	
MCBXFBH.A2R5						
MCBXFBV.B2R5	1.2 m	dip	BSHL_Q23	0.4 W	17.8 W	
MCBXFBH.B2R5						
MCBXFAV.3R5	2.2 m	dip	BSHL_Q23	0.7 W	31.6 W	
MCBXFAH.3R5						
Drifts	15.6 m	drift	BSHL_Q23	4.7 W	714.7 W	
Total IT R5						**1662.7 W**

Table D.2: Expected heat loads for the different elements of the inner triplet on the right side of IP5. The electron cloud contribution is evaluated for SEY=1.3.

Name	Length	Field config.	Chamber	Impedance (T_BS= 20 K)	e-cloud (SEY=1.1)	Total
ITQ1R8	9.8 m		BSMQ_Q1-R	5.2 W	0.9 W	6.1 W
MQXA.1R8	6.4 m	quad	BSMQ_Q1-R	3.5 W	0.9 W	
MCBXH.1R8						
MCBXV.1R8	0.5 m	dip	BSMQ_Q1-R	0.2 W	0.0 W	
Drifts	3.0 m	drift	BSMQ_Q1-R	1.4 W	0.0 W	
ITQ2Q3R8	23.7 m		BSMQ_2	9.3 W	72.2 W	81.5 W
MQXB.A2R8	5.5 m	quad	BSMQ_2	2.3 W	17.8 W	
MQXB.B2R8	5.5 m	quad	BSMQ_2	2.3 W	26.9 W	
MQXA.3R8	6.4 m	quad	BSMQ_2	2.6 W	27.4 W	
MCBXH.2R8						
MCBXV.2R8	0.5 m	dip	BSMQ_2	0.2 W	0.0 W	
MCBXH.3R8						
MCBXV.3R8	0.5 m	dip	BSMQ_2	0.2 W	0.0 W	
Drifts	5.4 m	drift	BSMQ_2	1.8 W	0.0 W	
ITD1R8	13.9 m		BSMB_1	4.2 W	15.2 W	19.4 W
MBX.4R8	9.5 m	dip	BSMB_1	3.0 W	14.0 W	
Drifts	4.4 m	drift	BSMB_1	1.2 W	1.2 W	
Total IT R8						**106.9 W**

Table D.3: Expected heat loads for the different elements of the inner triplet on the right side of IP8. The electron cloud contribution is evaluated for SEY=1.1.

Name	Length	Field config.	Chamber	Impedance (T_BS= 20 K)	e-cloud (SEY=1.3)	Total
ITQ1R8	9.8 m		BSMQ_Q1-R	5.2 W	197.7 W	202.9 W
MQXA.1R8	6.4 m	quad	BSMQ_Q1-R	3.5 W	191.4 W	
MCBXH.1R8						
MCBXV.1R8	0.5 m	dip	BSMQ_Q1-R	0.2 W	0.0 W	
Drifts	3.0 m	drift	BSMQ_Q1-R	1.4 W	6.3 W	
ITQ2Q3R8	23.7 m		BSMQ_2	9.3 W	573.0 W	582.3 W
MQXB.A2R8	5.5 m	quad	BSMQ_2	2.3 W	143.4 W	
MQXB.B2R8	5.5 m	quad	BSMQ_2	2.3 W	158.5 W	
MQXA.3R8	6.4 m	quad	BSMQ_2	2.6 W	161.3 W	
MCBXH.2R8						
MCBXV.2R8	0.5 m	dip	BSMQ_2	0.2 W	6.0 W	
MCBXH.3R8						
MCBXV.3R8	0.5 m	dip	BSMQ_2	0.2 W	8.3 W	
Drifts	5.4 m	drift	BSMQ_2	1.8 W	95.6 W	
ITD1R8	13.9 m		BSMB_1	4.2 W	281.4 W	285.6 W
MBX.4R8	9.5 m	dip	BSMB_1	3.0 W	163.4 W	
Drifts	4.4 m	drift	BSMB_1	1.2 W	118.1 W	
Total IT R8						**1070.8 W**

Table D.4: Expected heat loads for the different elements of the inner triplet on the right side of IP8. The electron cloud contribution is evaluated for SEY=1.3.

Bibliography

[1] L. Mether, "Electron cloud in 2016: cloudy or clear?." Proc. of the 7th Evian Workshop, Evian 13-15 Dec 2016 https://indico.cern.ch/event/578001/.

[2] G. Iadarola, "Filling schemes and e-cloud constraints." Proc. of the 7th Evian Workshop, Evian 13-15 Dec 2016 https://indico.cern.ch/event/578001/.

[3] G. Apollinari, I. Bejar Alonso, O. Bruning, P. Fessia, M. Lamont, L. Rossi, and L. Tavian, *High-Luminosity Large Hadron Collider (HL-LHC): Technical Design Report V. 0.1*. CERN Yellow Reports: Monographs 4/2017, Geneva: CERN, 2017.

[4] G. Iadarola, E. Metral, and G. Rumolo, "Beam induced heat loads on the beam-screens of the twin-bore magnets in the IRs of the HL-LHC." https://cds.cern.ch/record/2217217/files/CERN-ACC-2016-0112.pdf, 2016. CERN report CERN-ACC-2016-0112.

[5] R. Kersevan, V. Baglin, and G. Bregliozzi, "Coupled Simulations of the Synchrotron Radiation and Induced Desorption Pressure Profiles for the HiLumi-LHC Triplet Area and Interaction Points," in *Proceedings, 5th International Particle Accelerator Conference (IPAC 2014): Dresden, Germany, June 15-20, 2014*, 2014.

[6] R. Kersevan, "Synchrotron Radiation Distribution and Related Outgassing and Pressure Profiles for the HL-LHC Final Focus Magnets," in *Proceedings, 6th International Particle Accelerator Conference (IPAC 2015): Richmond, Virginia, USA, May 3-8, 2015*, 2015.

[7] A. Rossi, "Estimates of heat load from synchrotron radiation for HL-LHC," *Presentation at theABP-HSS Section meeting, 20 Apr 2016, CERN*.

[8] G. Iadarola, E. Belli, K. Li, L. Mether, A. Romano, and G. Rumolo, "Evolution of Python Tools for the Simulation of Electron Cloud Effects," in *Proc. of International Particle Accelerator Conference (IPAC'17), Copenhagen, Denmark, May, 2017*, JACoW.

[9] "Drawing Information: IR5 RIGHT, CELLS C1.R5 TO C7.R5." https://edms5.cern.ch/cdd/plsql/c4w_edms.edms_logon?jump=SEARCH&p1=DIRECT&p2=LHCLSXH_0010&p3=AD.

[10] "LHC Design Report (section 3.2.5)." https://edms.cern.ch/ui/file/445831/5/Vol_1_Chapter_3.pdf.

[11] "HiLumi LHC Work Package 3 - Magnets for Insertion Regions." https://espace.cern.ch/HiLumi/wp3/SitePages/Home.aspx.

[12] V. Baglin, "Review of vacuum design choices of all IRs, coated locations and materials, expected SEY." https://indico.cern.ch/event/647815/, Unpublished. Presentation at the 97th HiLumi WP2 Meeting.

[13] P. Dijkstal, "Higher order and skew magnets in PyECLOUD." https://indico.cern.ch/event/637703/contributions/2583367/attachments/1456196/2248943/dijkstal_ecloud42.pdf, Unpublished. Presented at Electron Cloud Meeting 42.

[14] N. Mounet, "Impedance considerations for the new hl-lhc triplet layout." Presentation at the 11th HiLumi WP2 Task Leader Meeting https://indico.cern.ch/event/259525/.

[15] "Animation of the electron dynamics inside an IR5 dipole." https://indico.cern.ch/event/625668/contributions/2527646/attachments/1433989/2237245/IR5_e_distribution_dip.mp4.

[16] "Animation of the electron dynamics inside an IR8 dipole." https://indico.cern.ch/event/625668/contributions/2527646/attachments/1433989/2204162/e_distribution_dipole.mp4.

[17] "Animation of the electron dynamics inside an IR5 quadrupole." https://indico.cern.ch/event/625668/contributions/2527646/attachments/1433989/2237247/IR5_e_distribution_quad.mp4.

[18] "Animation of the electron dynamics inside an IR8 quadrupole." https://indico.cern.ch/event/625668/contributions/2527646/attachments/1433989/2205081/e_distribution_quad.mp4.

[19] "Animation of the electron dynamics inside an IR5 drift." https://indico.cern.ch/event/625668/contributions/2527646/attachments/1433989/2237246/IR5_e_distribution_drift.mp4.

[20] "Animation of the electron dynamics inside an IR8 drift." https://indico.cern.ch/event/625668/contributions/2527646/attachments/1433989/2204160/e_distribution_drift.mp4.

[21] "Animation of the electron dynamics inside an IR5 sextupole." https://indico.cern.ch/event/625668/contributions/2527646/attachments/1433989/2354100/e_distribution_ir5_sextupole.mp4.

[22] "Animation of the electron dynamics inside an IR5 skew sextupole." https://indico.cern.ch/event/625668/contributions/2527646/attachments/1433989/2354101/e_distribution_ir5_sextupole_skew.mp4.

[23] "Animation of the electron dynamics inside an IR5 octupole." https://indico.cern.ch/event/625668/contributions/2527646/attachments/1433989/2354102/e_distribution_ir5_octupole.mp4.

[24] "Animation of the electron dynamics inside an IR5 skew octupole." https://indico.cern.ch/event/625668/contributions/2527646/attachments/1433989/2354103/e_distribution_ir5_octupole_skew.mp4.

[25] "Animation of the electron dynamics inside an IR5 decapole." https://indico.cern.ch/event/625668/contributions/2527646/attachments/1433989/2354104/e_distribution_ir5_decapole.mp4.

[26] "Animation of the electron dynamics inside an IR5 skew decapole." https://indico.cern.ch/event/625668/contributions/2527646/attachments/1433989/2354105/e_distribution_ir5_decapole_skew.mp4.

[27] "Animation of the electron dynamics inside an IR5 dodecapole." https://indico.cern.ch/event/625668/contributions/2527646/attachments/1433989/2354106/e_distribution_ir5_dodecapole.mp4.

[28] "Animation of the electron dynamics inside an IR5 skew dodecapole." https://indico.cern.ch/event/625668/contributions/2527646/attachments/1433989/2354108/e_distribution_ir5_dodecapole_skew.mp4.